BACHELOR THESIS

Study of the functioning and importance of diffusers in Formula 1 cars

Author:
Porcar Galan, Laura

Director:
Gamez Montero, Pedro Javier

REPORT

UNIVERSITAT POLITÈCNICA DE CATALUNYA

ESCOLA SUPERIOR D'ENGINYERIES INDUSTRIAL, AEROESPACIAL I AUDIOVISUAL DE TERRASSA

BACHELOR'S DEGREE IN AEROSPACE TECHNOLOGY ENGINEERING
COURSE 2019-2020

JUNE 30, 2020

Declaration of Authorship

I, Laura Porcar Galan, declare that this project titled, "Study of the functioning and importance of diffusers in Formula 1 cars" and the work presented in it are my own. I confirm that:

- This work was done wholly or mainly while in candidature for a research degree at this University.
- Where any part of this thesis has previously been submitted for a degree or any other qualification at this University or any other institution, this has been clearly stated.
- Where I have consulted the published work of others, this is always clearly attributed.
- Where I have quoted from the work of others, the source is always given. With the exception of such quotations, this thesis is entirely my own work.
- Where the thesis is based on work done by myself jointly with others, I have made clear exactly what was done by others and what I have contributed myself.

I understand that an infringement of this declaration leaves me subject to the foreseen disciplinary actions by *The Universitat Politècnica de Catalunya - BarcelonaTECH*.

Signed:

Date: 30th of June of 2020

Abstract

This project focuses on explaining and understanding the functioning of diffusers and their importance in Formula 1 cars. Formula 1 car diffusers are the most unexplored elements in these vehicles, since their interaction with the ground show a non-understood flow behaviour. First, an explanation of the fundamental aerodynamic concepts that govern the aerodynamics of these vehicles is presented in order to understand how the flow works on diffusers and how relevant their use in aerodynamic load generation is. In addition, understanding these concepts is essential to analyze the results obtained in subsequent flow simulations and analysis. An extensive research about experimental and numerical information about motorsport diffusers is done. The geometry of diffusers is studied to know which is the optimum geometry that reaches high level of performance on this elements. The theoretical approach is principally based on [8] and [7] due to its highly understandable and clear content about motorsport diffusers.

Once the functioning of diffusers has been analyzed and understood, CFD simulations of an approximate diffuser geometry are performed. The geometry simulated is the Ahmed body, a geometry that is used as a model that simulates the flow behaviour of motorsport diffusers. Three different Ahmed body configurations are performed: 0° diffuser, 25° diffuser and in the third case rear airfoils are added to the 25° diffuser Ahmed body. Simulation boundary conditions are determined taking into account the wall contour conditions. One of the parameters to be studied is the value of lift coefficient, which shows the aerodynamic load of the car, that is, the vertical force that causes the car to adhere to the ground and, hence improve cornering and acceleration performance. These analysis are performed with open-source CFD simulation software OpenFOAM©. Since there is no previous experience with this type of software, a stage of familiarization is done beforehand. An analysis of the results is done relating these results with the theoretical approach, as well as making a comparison between the 3 simulations. It is obtained that the 25° diffuser configuration generated more downforce than the 0° diffuser, which makes sense as the aim of adding a diffuser is to increase the amount of downforce produced. In addition, the 25° diffuser Ahmed body with the rear airfoils results in an substantial increase of downforce thank to the low pressure zone generated at the back of the body with the help of these airfoils. Finally, a study of the project costs will be performed as well as an environmental impact study.

Resumen

Este proyecto se centra en explicar y comprender el funcionamiento de los difusores y su importancia en los coches de Fórmula 1. El difusor es el elemento más inexplorado de un coche de Fórmula 1, ya que su interacción con el suelo presenta un comportamiento de flujo que no es del todo comprendido. En primer lugar, se presenta una explicación de los conceptos aerodinámicos fundamentales que rigen la aerodinámica de estos vehículos con el objetivo de comprender cómo funciona el flujo en los difusores y cuán relevante es su uso en la generación de carga aerodinámica. Además, comprender estos conceptos es esencial para analizar los resultados obtenidos en las simulaciones que se realizan posteriormente. Se realiza una extensa investigación sobre información experimental y numérica sobre difusores de automovilismo. Además, se estudia la geometría de los difusores para así poder entender cómo variar la geometría para obtener un alto nivel de rendimiento y eficiencia de este elemento aerodinámico. El enfoque teórico se basa en los artículos [8] y [7] debido a su contenido altamente comprensible y claro sobre los difusores de automovilismo.

Una vez que se ha analizado y comprendido el funcionamiento de los difusores, se hacen simulaciones de CFD de tres geometrías aproximadas del difusor. Esta geometría está basada en el *Ahmed body*, cuerpo que se utiliza para representar aproximadamente la forma de un coche y, añadiendo un difusor en la parte trasera se puede simular el flujo que estos generan. Las tres geometrías son: difusor de 0°, difusor de 25° y, por último, la configuración con el difusor de 25° añadiendo un perfil alar a cada lado del difusor. Las condiciones de contorno se determinarán teniendo en cuenta las condiciones del contorno del muro. Uno de los parámetros a estudiar es el valor del coeficiente de sustentación, que muestra la carga aerodinámica del automóvil, es decir, la fuerza vertical que hace que se adhiera al suelo y, por lo tanto, mejore el rendimiento y la aceleración en las curvas. Estos análisis se realizan con el software de simulación CFD OpenFOAM©. Como no hay experiencia previa con este tipo de software, se debe realizar una etapa de aprendizaje del software. En el análisis de los resultados se relacionan estos resultados con el enfoque teórico, además de comparar los resultados entre las 3 simulaciones. Se obtiene que la configuración del difusor de 25° genera más carga aerodinámica que el difusor de 0°, fenómeno que es razonable ya que el objetivo de añadir un difusor es aumentar la carga aerodinámica en el cuerpo. Además, el *Ahmed body* con difusor de 25° con los perfiles en la parte trasera genera un aumento sustancial de la carga aerodinámica gracias a la zona de baja presión que se genera en la parte posterior del cuerpo con la ayuda de estos perfiles. Finalmente, se realiza un estudio de los costos del proyecto, así como un estudio de impacto ambiental.

Acknowledgements

Foremost, I would like to express my special thanks of gratitude to my project advisor Pedro Javier Gámez Montero for believing in me and giving the opportunity to do this project on the topic I have great interest in. I also would like to thank him for the continuous support, for his patience and advices and for helping me when I was in a hard-time stage of the project. His guidance helped me in all the time of research and writing of this thesis. I am also grateful to professor Robert Castilla who has provided part of his time helping me understand the use of OpenFOAM©.

I would like to make a special mention to Willem Toet, former Formula 1 aerodynamics engineer, who took time of his own to make me understand as much as possible how Formula 1 cars diffusers worked. Furthermore, he suggested the idea of doing a CFD simulation with the rear airfoils, case that really gives the special thing that this project offers to the investigation about F1 diffusers.

Last but not the least, I would like to thank my family and friends for supporting in difficult times. A special thank to my parents for their sacrifice for providing me the best education possible and preparing me for the future.

Contents

List of Figures

List of Tables

Nomenclature

A	Cross-sectional area	m^2
AR	Aspect ratio	
CFD	Computational Fluid Dynamics	
C_D	Drag coefficient	
C_L	Lift coefficient	
C_L/C_D	Aerodynamic efficiency	
C_p	Pressure recovery coefficient	
C_{p_1}	Inlet pressure coefficient	
C_{p_2}	Outlet pressure coefficient	
$\overline{C}_{p_d}$	Flat-underbody surface mean-effective pressure coefficient	
$\overline{C}_{p_f}$	Diffuser surface mean-effective pressure coefficient	
$\overline{C}_{p_l}$	Lower surface mean-effective pressure coefficient	
$\overline{C}_{p_u}$	Upper surface mean-effective pressure coefficient	
F_D	Force of drag	N
F_L	Force of lift	N
h	Ride height	m
H	Ahmed body height	m
h/H	Non-dimensional ride height	
I	Turbulence intensity	
k	Turbulent kinetic energy (TKE)	$J/kg = m^2/s^2$
L	Ahmed body length	m
N	Diffuser length	m
N/h	Non-dimensional diffuser length	
N/L	Non-dimensional diffuser length	
p	Pressure	Pa ($kg\,m^{-1}\,s^{-2}$)
S	Reference surface	m^2
SA	Spalart-Allmaras	
SST	Shear Stress Transport	
U	Velocity	m/s
u	Velocity	m/s
v	Velocity	m/s
W	Ahmed body length	m
Γ	Circulation	m^2/s
θ	Diffuser slant angle	$^\circ$
μ	Molecular dynamic viscosity	kg/m·s
μ_t	Turbulent dynamic viscosity	kg/m·s
ν	Kinematic viscosity	m^2/s
ρ	Density	kg/m^3
ω	Turbulence specific dissipation rate	1/s
	Vorticity	1/s

Dedicated to my family and friends who have always believed in me.

1 Introduction

1.1 Background

First of all, one of the main motivations on the realization of this project is to be able to understand more in detail the functioning of the diffusers in Formula 1 cars, as the front and rear wings are always given more importance. On the other hand, carrying out this project gives the opportunity to learn how to do CFD simulations, which will eventually be useful in the automotive or aerospace field if future career is headed towards these fields of work. Furthermore, these simulations will give very relevant information about the aerodynamics desired to study and comprehend, for instance the velocity around the diffuser.

On a personal level, Formula 1 is a field that I have always had interest in and have always watched on television. However, there are aspects hard to understand, especially with regard to the aerodynamics of the vehicles. This is why this project is an opportunity to understand all the aerodynamic concepts that govern the world of racing cars, specially Formula 1 cars. Hence, it is a topic that I would carry out with motivation and desire.

Before starting the project, an article about motorsport diffusers [27], written by former Formula 1 aerodynamics engineer Willem Toet, was found and read. As the article showed great knowledge about Formula 1 diffusers, the idea of contacting the writer came up. Willem Toet was contacted by LinkedIn and the following information was given:

"Diffusers work best in ground effect but you have to be careful that they have 'enough' air. There are many tricks used to ensure we keep energy available near the expanding surface of the diffuser."

Additionally, Willem kindly offered himself to answer any questions that came out about diffusers in Formula 1 during the realization of the project. He has been working several years on the development of these elements, thus his help will be very helpful. Besides, he provided a rather interesting article [16] about the vortices generated in diffusers which will be used for the theoretical approach of the project, as well as the articles about Formula 1 diffusers written by Willem.

1.2 Objectives of the project

The main tasks to be carried out in this project are:

- Acknowledge in detail the use and importance of diffusers in Formula 1 cars
- Learn to use CFD thoroughly
- Explain the obtained results clearly so that a Formula 1 fan who is not an aerodynamics expert can understand the concepts explained

- Work in the study and analysis of fluid simulations involving real engineering problems
- Determine feasibility of the engineering project to be carried out
- Study the socio-economics aspects in fluid dynamics applications solved by numerical simulation and fields of interest

1.3 Scope of the project

- Detailed explanation of the functioning of Formula 1 car diffusers.
- Understanding of the aerodynamics of Formula 1 car diffusers.
- CFD simulations of the Ahmed body, representation of a motorsport diffuser.
  - Pressure and velocity distribution of the airflow around the body.
  - Determination of downforce and drag forces on the body.
- A budget of the project will be presented so as to determine the feasibility of the project.
- An environmental impact of the project done will be presented.
- Planning about the organization of the project realization (Gantt chart).

1.4 Requirements

The principal requirements needed for this project are presented below:

- Basic knowledge on fluid mechanics and CFD.
- As the project is about Formula 1 cars, basic knowledge of the corresponding aerodynamic elements, specially diffusers. Being familiar with these elements and slightly know how they affect the performance of these race cars will help carrying out the study.
- Basic knowledge of Solidworks©.
- Have great interest and motivation towards the project, try to contact Formula 1 teams or the engineers working in the aerodynamics of these cars would be very helpful to fully understand this aerodynamic element.
- Information research, find and read papers, scientific articles, technical data...

2 Fundamentals of aerodynamics

In order to understand the functioning and flow physics of a motorsport diffuser, the fundamentals of aerodynamics that govern the flow must be exposed. Without the knowledge of these aspects, it would be very difficult to understand the flow behaviour around a diffuser. Several aerodynamics concepts will be described in the following sections.

2.1 Flow definition

Flow is the term that refers to the movement of a fluid. There are several types of defining flows, which is important to know when studying a certain flow. [15]

2.1.1 Steady and Unsteady flow

Steady flow, or stationary flow, is the type of flow in which the properties of the fluid (velocity, pressure...) at a particular fixed point does not change with time.

Moreover, an unsteady flow is the type of flow where the properties do depend on time, they change for each instant of time.

2.1.2 Inviscid and viscous flow

In an inviscid flow, viscosity is not important so it can be neglected. Whilst, in a viscous flow viscosity play a huge role in the flow characteristics, hence it can not be ignored. In order to determine the importance of viscosity, the Reynolds number is a good indicator.

$$Re = \frac{\rho U l}{\mu} = \frac{\text{inertial forces}}{\text{viscous forces}} \tag{2.1}$$

This Reynolds number compares inertial and viscous forces (see Eq. 2.1), and depending on the result viscosity can be neglected or not. For Re » 1, inertial forces prevail infront of viscous forces, hence viscous forces are negligible and it can be approximated to an inviscid flow. Whereas Re « 1 means that viscous forces are greater than inertial and viscosity can not be neglected. When studying a flow around solid surface, the region of the flow away from the body can be considered inviscid, but thin region immediately in contact with the surface is a viscous flow. This viscous region is called boundary layer and is it explained in Sec. 2.2.

2.1.3 Compressible and incompressible flow

In incompressible flows, fluid flow's density can be considered constant. On the other hand, compressible flow is the one that suffers a variation in density. Fluids can classified depending on the Mach number. The Mach number M is the relation

between the velocity of the fluid U with respect the speed of sound c. Its definition is in Eq. 2.2.

$$M = \frac{U}{c} \tag{2.2}$$

A fluid can be considered incompressible if the number of Mach is $M < 0.3$, which is an important aspect when solving a fluid mechanics problem as this approximation reduces the complexity of a problem. In case of compressible flow, Bernoulli's equation is not applicable since the assumption for Bernoulli's equation is that density ρ is constant.

2.1.4 Uniform and non-uniform flow

Uniform flow is the one in which velocity and other properties are constant independent of directions, constant on all the flow path. Normally, it is assumed that free stream flow, far away from an aerofoil or a car, is a uniform flow.

In non-uniform flow, the flow parameters vary and are different at different points on the flow path.

2.1.5 One, two and three dimensional flow

All fluid flows are usually three-dimensional, fluid properties change in the three coordinates. However, for simplicity purposes, simplifications on the number of space coordinates can be applied. Usually fluid flow properties can be considered constant in certain coordinate directions. Depending on which coordinate direction excluded, there are 3 types of flows:

- In one-dimensional flow, its characteristics only depend on time and one space coordinate.
- In two-dimensional flow, its characteristics depend on time and two space coordinates.
- In three-dimensional flow, its characteristics depend on time and the three space coordinates.

2.1.6 Laminar and turbulent flow

Laminar flow, in which the streamlines are smooth and regular and a fluid element moves smoothly along a streamline.

In a turbulent flow streamlines break up and fluid moves in a random and irregular way. The velocity remains approximately close to the free-stream velocity, then at the surface it rapidly decreases to zero. In contrast, the laminar velocity profile gradually decreases to zero from the outer edge to the surface. In turbulent flows, inertial forces are dominant over viscous forces, hence the Reynolds number is very large.

2.1.7 Rotational and irrotational flow

A rotational flow is the one in which the angle between the two intersecting lines of the boundary of the fluid element changes while moving in the flow. Whereas an

irrotational flow is the one where the fluid element rotates as a whole and there is no change in angles between the boundary lines.

2.2 Boundary layer

A boundary layer is a thin layer of viscous fluid that appears when close to a solid surface in contact with a moving stream. Flow velocity within boundary thickness varies from zero at the wall —due to non-slip condition— and up to the free stream velocity U_∞. Fluid takes the velocity the surface has; if this wall has 0 velocity, the fluid touching the wall will have 0 velocity because of the shear stress at the wall, and as far from the solid, the boundary layer's thickness increases. This high shear stress at the surface reduces as far from the solid, which produces the transition from zero velocity at the solid to free-stream velocity away from it, forming the boundary layer.

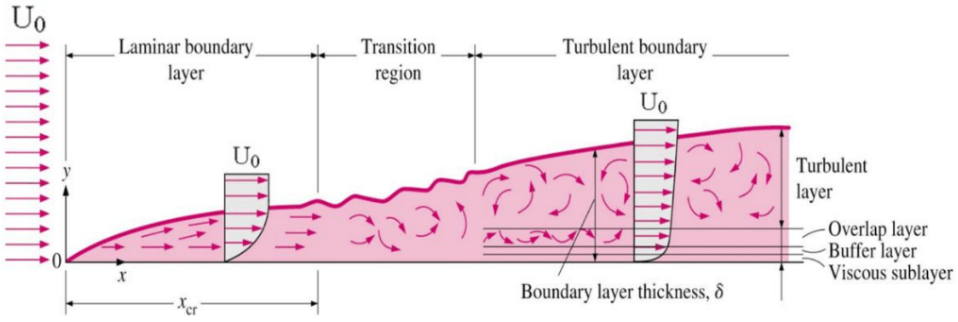

FIGURE 2.1: Scheme of boundary layer. Extracted from [4]

In boundary layers, the flow can be either laminar, transitional from laminar to turbulent or turbulent. As shown in Fig. 2.1, at the beginning, boundary layer normally develops as a laminar flow, but if it grows for enough distance along the surface it abruptly becomes turbulent. The value of Re_x can be defined in order to know from which critical number of Reynolds the boundary layer might transition to turbulent boundary layer. [23]

$$Re_x = \frac{\rho U x}{\mu} = \frac{U x}{\nu} \tag{2.3}$$

Where ρ is the airflow density, U is the velocity, x is the position in the x-direction, μ and ν are the dynamic and kinematic viscosity, respectively. When reaching this critical value of the Reynolds number, the laminar boundary layer is very unstable and can become turbulent. Normally, transition from laminar to turbulent occurs when $Re_x > 10^6$. [4]

2.2.1 Boundary layer separation

The separation of the boundary layer is the detachment of the boundary layer from the solid surface. That provokes areas where the particles of fluid move arbitrarily. This separation is usually the consequence of the changes in the geometry and the Reynolds number. Pressure gradient is one of the factors that influences on the development of a flow. It is easy to see in Fig. 2.2 that the shear stress on the surface caused by viscosity has a retarding effect upon the flow. This effect can however

be overcome if there is a negative pressure gradient offered to the flow. A negative pressure gradient is called *favourable pressure gradient*, since it helps the flow develop and move forward the surface without reversing. Nevertheless, a positive pressure gradient has the opposite effect causing a strong flow deceleration and is called the *adverse pressure gradient*. In Fig. 2.2, this adverse pressure gradient appears in last the stage presented, in which the flow begins to retard. From this moment, the shear stress becomes negative, the flow reverses and a region of recirculating flow develops, thus leading to flow separation. When the flow separates from the surface, it abruptly changes the pressure distribution over the surface causing an increase in drag called pressure drag. [22]

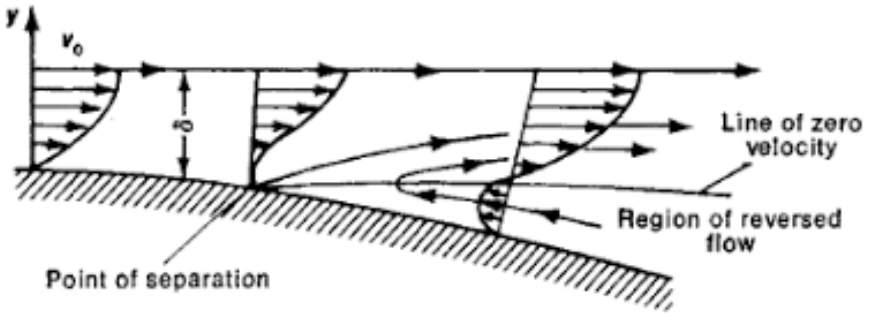

FIGURE 2.2: Scheme of boundary layer separation. Extracted from [3]

Another consequence of flow separation is the formation of a wake composed of the region of strong turbulence developed on the separation surface. Sometimes the recirculating flow zone disappears and the flow can reattach to the surface forming a separation bubble. This reattachment may be due to a favourable pressure gradient, which can appear thanks to body geometry and other. Another aspect that could help this reattachment is that the flow initially laminar, in the bubble could occur a transition to become turbulent. A turbulent flow has more energy and momentum than a laminar flow, which can stop separation and help flow reattach to the body.

2.3 Venturi's effect

The Venturi effect states that a fluid in a lower pressure zone will have a higher velocity, while in a higher pressure zone the velocity will be lower. This is done in order to keep the overall energy of the fluid constant, considering no energy losses and for the case of incompressible fluid. This effect can be seen for instance when going to a concert. If the doors to enter to the arena are big, a great amount of people are able to enter at the same time. However, if the doors are very small, less people are able to enter at the same time, and people have to enter with a higher rate or velocity through this smaller door so as the same amount of people can enter the arena in the same time as it the larger door. This effect occurs along with mass conservation for an incompressible fluid.

2.4 Ground effect

Ground effect is an aerodynamic effect that occurs when a body is brought close enough to the ground. Ground Effect is the art of creating a low pressure area underneath the car so that the atmospheric pressure pushes the car to the ground, which is the reverse of what happens with an aircraft wing. As the body gets closer to

ground proximity, the cross sectional area available for the air passing between it and the ground shrinks, making the flow to accelerate, creating flow asymmetry on the body, and as a result pressure underneath the body is reduced – in accordance with the Bernoulli principle – while the pressure on top doesn't change, and results in a force acting downwards on the body. In particular, low pressure could be created underneath the car by using the ground plane almost like the floor of a Venturi duct. The Bernoulli principle is not the only mechanic in generating ground effect downforce, but major ground effect performance comes from taking advantage of viscosity. The boundary layer between the corresponding two surfaces slows down the air between them, thing that reduces the Bernoulli effect. As the ground moves, it pulls on the air above it and causes it to move faster. This enhances the Bernoulli effect and increases downforce. This effect is a consequence of the distortion of the airflow below such surfaces due to the proximity of the ground.

2.5 Governing equations

The most significant equations in fluid mechanics that govern fluid flows are presented in this section.

2.5.1 Mass conservation equation

The amount of mass remains constant as mass is neither created nor destroyed.

$$\frac{\partial \rho}{\partial t} + \bigtriangledown \cdot (\rho \vec{V}) = 0 \tag{2.4}$$

The first term represents the change in density with time and the second is the convective term, flow of mass through boundaries.

2.5.2 Navier-Stokes equations

The Navier-Stokes equations are the differential equations that describe the flow of incompressible fluids. They describe how the velocity, pressure, temperature and density of a fluid are related. These equations are very difficult to solve. They are usually solver by CFD simulations.

$$\rho \left(\frac{\partial u}{\partial t} + u\frac{\partial u}{\partial x} + v\frac{\partial u}{\partial y} + w\frac{\partial u}{\partial z} \right) = \rho g x - \frac{\partial p}{\partial x} + \mu \left(\frac{\partial^2 u}{\partial x^2} + v\frac{\partial^2 u}{\partial y^2} + w\frac{\partial^2 u}{\partial z^2} \right) \tag{2.5}$$

$$\rho \left(\frac{\partial v}{\partial t} + u\frac{\partial v}{\partial x} + v\frac{\partial v}{\partial y} + w\frac{\partial v}{\partial z} \right) = \rho g y - \frac{\partial p}{\partial y} + \mu \left(\frac{\partial^2 v}{\partial x^2} + v\frac{\partial^2 v}{\partial y^2} + w\frac{\partial^2 v}{\partial z^2} \right) \tag{2.6}$$

$$\rho \left(\frac{\partial w}{\partial t} + u\frac{\partial w}{\partial x} + v\frac{\partial w}{\partial y} + w\frac{\partial w}{\partial z} \right) = \rho g z - \frac{\partial p}{\partial z} + \mu \left(\frac{\partial^2 w}{\partial x^2} + v\frac{\partial^2 w}{\partial y^2} + w\frac{\partial^2 w}{\partial z^2} \right) \tag{2.7}$$

The terms on the left hand side are called convection terms. They represent the change of velocity with time and the inertial term, respectively. The terms on the right hand side are the diffusion terms: body forces, pressure and viscosity contributions, respectively following the order in the previous equations.

2.5.3 Bernoulli equation

The Bernoulli equation establishes a relationship between the pressure of a fluid to its velocity. The hypothesis that this equation takes into account are: incompressible fluid and steady and irrotational flow.

$$p_1 + \frac{1}{2}\rho v_1^2 + \rho g h_1 = p_2 + \frac{1}{2}\rho v_2^2 + \rho g h_2 + losses \tag{2.8}$$

Where p is the static pressure, ρ the density of the air flow, u the velocity of the air flow, g the gravity, h the height of the fluid and the *losses* are due to friction. The first term represents the pressure energy, the second the kinetic energy of the fluid and the third term the potential energy. In the case of a Formula 1 it could be considered that the properties of the air do not vary with height (potential energy can be neglected) and that there are no losses of heat or work. Hence Eq. 2.9 is obtained.

$$p_1 + \frac{1}{2}\rho v_1^2 = p_2 + \frac{1}{2}\rho v_2^2 \tag{2.9}$$

It can be observed that as the energy remains constant along a streamline, if the pressure is lower, the contribution of the kinetic energy, hence the velocity, has to be greater, in the same way that if there is an increase of pressure there will be a decrease in velocity. This phenomenon is what governs the profiles: when air is made to flow around a non-symmetrical body, simply because it is not symmetrical, the flow of air will surround the body differently from the upper surface than from the lower surface, which will lead to velocity difference between both surfaces and therefore a difference in body pressures. The particles circulating above, make a longer distance than those circulating below to reach the other side at the same time. Consequently, to reach the other side the particles circulating at the top must have a higher velocity. Observing Eq. 2.9, it is deduced that a higher velocity implies a lower pressure and this pressure difference that is created between the surfaces is what generates a lifting force. In the case of Formula 1 cars, this lifting force is directed downwards and is the so-called aerodynamic load of downforce.

2.6 Aerodynamic forces and coefficients

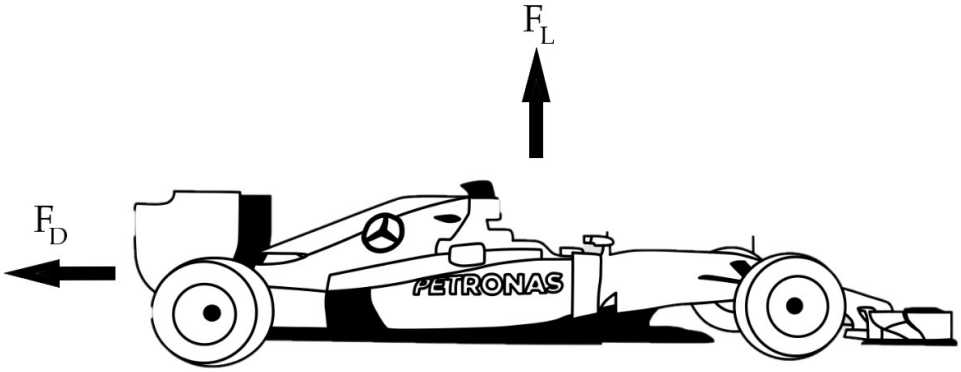

FIGURE 2.3: Scheme of the forces acting on a vehicle

When a solid object travels trough the air, aerodynamic forces appear acting on it. The two main forces that appear are the lift and drag forces, as shown in Fig. 2.3. Lift is the force that acts on a vehicle normal to the road surface that the vehicle rides on. This vertical force usually has the effect of "pulling" the vehicle upwards - away from the surface it drives on. However, in the case of vehicles, creating a negative lift acting downwards is what is needed to improve the adhesion of the tires to the ground. This negative lift $-C_L$ is called *downforce*. Increasing this downforce, improves the cornering force which enables the vehicle to go around corners faster and reduce lap times. This lift coefficient is characterized by the lift coefficient C_L as defined in Eq. 2.10.

$$F_L = \frac{1}{2}\rho \mathrm{U}^2 S C_L \tag{2.10}$$

The other aerodynamic force is the drag. Drag is the aerodynamic resistance, acting opposite to a object's motion, that a solid object experiences when traveling trough the air. It acts as a limit of the top speed of a vehicle and increases the fuel consumption. For this reason, it is interesting to make the vehicles aerodynamically efficient so as to reduce fuel consumption and get to high velocities. For street cars, this drag-reduction has the principal aim of reducing the fuel consumption on the car, reducing the cost of fuel of the car, hence decreasing the pollution. This force is defined by Eq. 2.11.

$$F_D = \frac{1}{2}\rho \mathrm{U}^2 S C_D \tag{2.11}$$

The drag force is characterized by the drag coefficient C_D and can appear as the resistance produced by pressure differential or by skin friction. The skin friction drag is produced by the contact of the fluid particles with a surface of a moving or fixed object. When these fluid particles get close to a surface, the particles closest to the body adhere to the surface. The particles passing over these attached particles slide over them with higher velocity than these particles at the surface, but The layer above these attached particles slides over them, but consequently they are also slowed down by the still particles on the surface. For this, as further from the object's surface, the velocity of the particles increase gradually until reaching the value of the free-stream velocity. This phenomenon produces the appearance of the boundary layer, this is why this type of drag is also called boundary layer drag.

3 Literature Review

A diffuser is a device which is fundamentally used to slow down the air velocity resulting in an increase in static pressure. As explained in previous Chapter 2 this effect is caused by the Venturi effect (see Sec. 2.3) with the application of the Bernoulli equation and mass conservation (see Sec. 2.5) in the case of an incompressible flow. The most important characteristic of a diffuser which makes its functioning possible is that its cross-sectional area increases from its inlet to exit planes, and from the continuity principle (see Chapter 2), with the increase of the cross-sectional area the air velocity decreases and its pressure increases. [11] A 2-dimensional scheme diffuser is shown in Fig. 3.1. This airflow device presents two main difficulties related to fluid-mechanics. On one hand, if the rate of diffusion is too high the boundary layer tends to separate from the diffuser walls, hence, resulting in a flow mix and large losses in stagnation pressure. On the other hand, if the diffusion rate is too low, the fluid is exposed to a long length of wall and fluid friction losses again become important. Therefore, the main objective is to find an optimum condition between the two cases exposed previously for which the losses are minimized. [9]

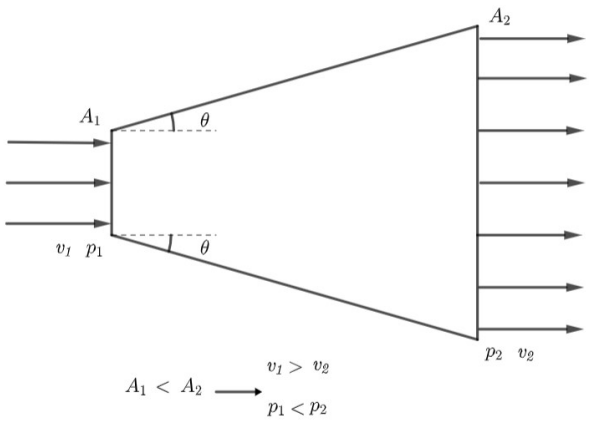

FIGURE 3.1: Scheme of a 2-dimensional diffuser

Fixing a certain area ratio, one of the parameters that influence the most the diffuser performance is its length. If the diffuser is too long, the pressure loss increases due to frictional effects. Moreover, if the length is too short, the decelerating flow will separate from the diffuser walls due to the appearance of an adverse pressure gradient which would lead to stall, causing higher pressure losses. [9] An important aspect when designing a diffuser is to achieve the diffusion in the shortest possible length, thus with the lowest pressure loss.

For certain inlet pressure coefficient C_{p_1} and outlet pressure coefficient C_{p_2}, the performance of a diffuser is given by its pressure recovery coefficient C_p, presented in Eq. (3.1).

$$C_p = \frac{C_{p_2} - C_{p_1}}{1 - C_{p_1}} \tag{3.1}$$

This coefficient shows the increment of pressure produced by the diffuser between the inlet and outlet. It is generally influenced by the diffuser ramp angle θ and inlet and outlet conditions. [11]

3.1 Formula 1 car diffuser

Formula 1 cars contain several elements to generate downforce so as to generate a suction and push the car's tires onto the road to enhance traction in track corners. The three most important elements in F1 cars are the front wing, the rear wing and the ground-effect diffuser. However, this study centers in the diffuser of Formula 1 cars as they are the most unknown part of the car. Additionally, the flat bottom along with the diffuser on Formula 1 cars are the elements that generate a great amount of downforce with less drag generation as shown in Fig. 3.3, where the downforce generation of these elements is about 60% of the total downforce, whereas only contribute to 10-20% of the drag on the car. This supposes an advantage compared to other elements such as front and rear wings that have a higher drag-to-downforce ratio.

The flat bottom of a Formula 1 car acts as a Venturi taking the air from the free stream to the underbody resulting in higher velocity relative to the air above the car, as shown in Fig. 3.2. If mass conservation is applied for an incompressible fluid, a reduction in the cross-sectional area implies an increase in the velocity of the flow, hence a reduction in the pressure. As stated on Bernoulli's Equation (see Chapter 2), when velocity increases, pressure decreases. This effect produces a pressure differential between the bottom (lower pressure) and top (higher pressure) of the car which manifests as increased load on the tires, also called downforce. [24]

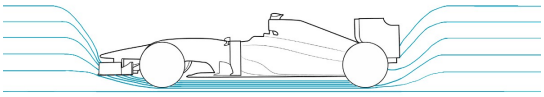

FIGURE 3.2: Venturi effect in the flat bottom of a Formula 1 car

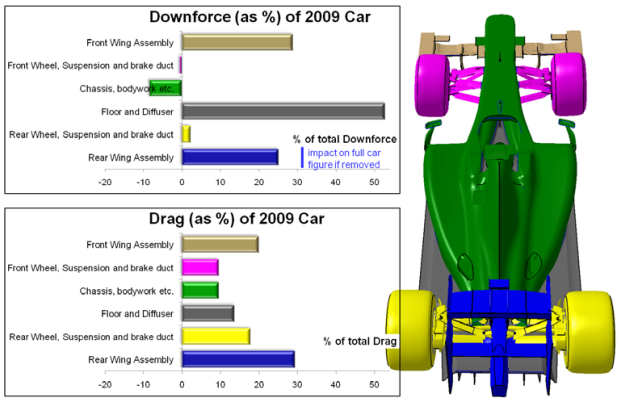

FIGURE 3.3: Downforce vs. drag. Extracted from [10]

To reduce the underbody pressure further, a diffuser is placed at the rear section of the car underbody and it consists of a diverging ramp surface. The diffuser's cross-sectional area increases until reaching its maximum area at the rear part of the bottom of the car, acting as a transitional section where the underbody airflow at high velocity and low pressure recovers the pressure before exiting to reintegrate at the free stream with atmospheric pressure.

The main role of the diffuser is to slow the air flowing under the car

and reintegrate this airflow smoothly to the free stream with higher-pressure ambient air (atmospheric pressure) at the diffuser exit. Smoothing the transition between the air from under the car and the ambient air is a crucial aspect since it reduces turbulent behaviour and drag in the car's wake and improves airflow enetering on the underbody of the vehicle. The principal objective is to implement the highest possible angle of the diffuser without having flow separation, since this flow separation may generate more drag and, hence reduce the amount of downforce. [13] An important parameter to consider is the pressure recovery of the diffuser. This parameter determines the magnitude of the pressure under the car, in other words, provides the pressure underneath the car compared to the atmospheric pressure above the car, thus determining the performance of the diffuser (see Sec. 3.5). [11]

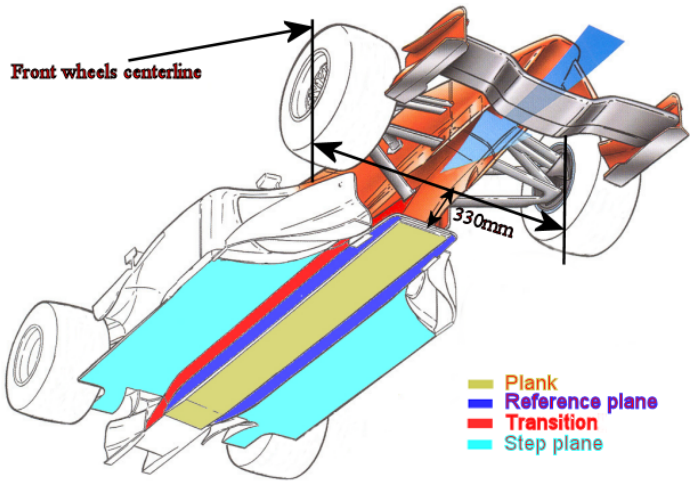

FIGURE 3.4: Parts of a Formula 1 car undertray. Extracted from [19]

Formula One undertrays show particular characteristics which enable the generation of downforce on the car. Nevertheless, these characteristics are defined by FIA technical regulations which are updated yearly, for the start of each season. F1 car of each season has its own technical regulations since every year the characteristics of the car may change with the aim of enhancing the performance of the car and making the sport more interesting for the spectators and the teams. Generally, Formula 1 car undertray configuration consists of the elements defined below and shown in Fig. 3.4. [25]

- PLANK. It is responsible of avoiding contact of the car's underbody with the track ground. It was introduced to guarantee a minimum ride height, thus avoiding teams getting advantage of ground clearances to improve diffuser performance.
- REFERENCE PLANE. It is the lowest part of the bottom of the car – excluding the plank– and runs along the centre of the car. It is used as a reference for defining all the heights of the car.
- TRANSITION. Undertray's element located between the reference plane and step plane.
- STEP PLANE. It is the part of the car's floor with larger surface, which generates over a third of the car's downforce, working best the closer to the ground, being one of the most regulated component by FIA.

– DIFFUSER. It was added in order to create downforce, since without this element, the bottom of the car would be flat and would create lift rather than downforce. As defined at the beggining of the section, it is located at the rear section of the undertray and as a general definition, it creates a higher pressure differential between the bottom and the top of the car. Additionally, vertical fences (or strakes) can be added to the diffuser with the objective to guide airflow into and out of the diffuser to maximize its efficiency.

Notwithstanding, for the further study in this paper these elements won't be considered, as the flow physics of the diffuser itself would become harder to understand. Once the functioning of the diffuser is acknowledged, these elements can be added in order to know how each of them influence on the generation of downforce. Nevertheless, these elements won't be studied in this paper. Studying or simulating the whole Formula 1 car requires high computational resources and much time to obtain good results. For this reason, a model that simulates the behaviour of flow around a car is considered for this study. The corresponding geometry is the Ahmed body and is introduced in the following Sec. 3.2.

3.2 Ahmed body

The Ahmed body is a standard geometry used to study bluff body flows first proposed by Ahmed and Ramm in 1984 [2]. It is used as a simplified vehicle model to commonly study flow behaviour on the underbody and on ground effect. Despite its simple shape (see Fig. 3.5), the Ahmed body allows us to see characteristic features that are relevant to bodies in the automotive industry, as well as provides a model to study geometric effects on the wakes of ground vehicles. This model is also used to describe the turbulent flow field around a car representative geometry. [11] [17] It presents the following dimensions: length (L) of 1.044m, height (H) of 0.288m and width (W) of 0.389m, with curvature radius at the front face of 0.1m. Additionally, as shown in Fig. 3.5, the addition of a diffuser in the rear part of the Ahmed body, 4 characteristic parameters appear: slant or diffuser angle θ, diffuser length N, ride height or inlet height h and outlet height h_2.

In [27], Willem Toet explains the fundamentals of diffusers in race cars based on his experience working with these devices. He states that the best performance of diffusers is given by 3-dimensional flow. Therefore, although the typical approximation of 2-dimensional flow is accepted for simpler geometries as the one in Fig. 3.5 or for first approximations, diffusers 3-D would be better to truly understand the functioning of Formula 1. Hence, this 3-dimensionality implies the appearance of vortices on different flow phases, which can be a great advantage when it comes to the creation of downforce.

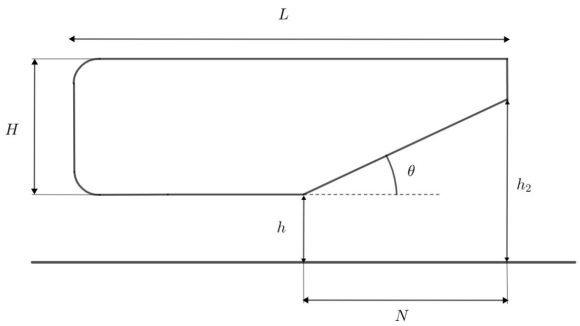

FIGURE 3.5: Parameters of an Ahmed body with a ground-effect diffuser. Extracted from [8]

In the present study, both 2-dimensional and 3-dimensional studies of the Ahmed body are performed in Chapter 4 in order to observe the behaviour of the flow under different diffuser configurations.

3.3 Experimental research

The diffuser of a Formula 1 car is the most unknown and non-understandable element of the vehicle since the flow passing through it is not fully predictable and determined. Therefore, it is worth understanding the flow physics behind this part. For this reason, a research of several experimental studies done on this field has been done so as to extract some conclusions.

In [8], wind-tunnel tests of the Ahmed body are performed. Two diffuser lengths of 25% and a 75% of the total length of the model are tested varying their ride height and diffuser angle, both of these parameters affecting the area ratio. The angle of the diffuser was in the range of 0-15° and ride height from 0-230 mm. The speed of the free stream airflow was of 30 m/s.

When studying the values of downforce, it is noticeable that for almost all the diffuser angles tested, if the ride height decreases, downforce increases until reaching a maximum at a small value of ride height: $h/H = 0.062$, specifically $h = 10\ mm$ from ground. For ride heights below this value, downforce decreases rapidly. It is stated by Cooper et al. [8] that the minimum value of downforce would be consequence of viscous effects appearing at small ride heights, where the boundary layer thickness in the diffuser wall takes more significance – see Sec. 2.2. Of all the slant angles tested, maximum downforce appeared for $\theta = 9.54°$ with a lift and drag coefficients of $C_L = -0.86$ and $C_D = 0.345$, see Fig. 3.6. Moreover, with respect to the drag behaviour, it resulted that drag is reduced due to underbody upsweep at high ride heights, and viceversa. From experimental results, the drag force begins to increase at the ride-height region where the downforce increases rapidly. Cooper et Al. found that drag reduction can be obtained when implementing short shallow-angle diffusers.

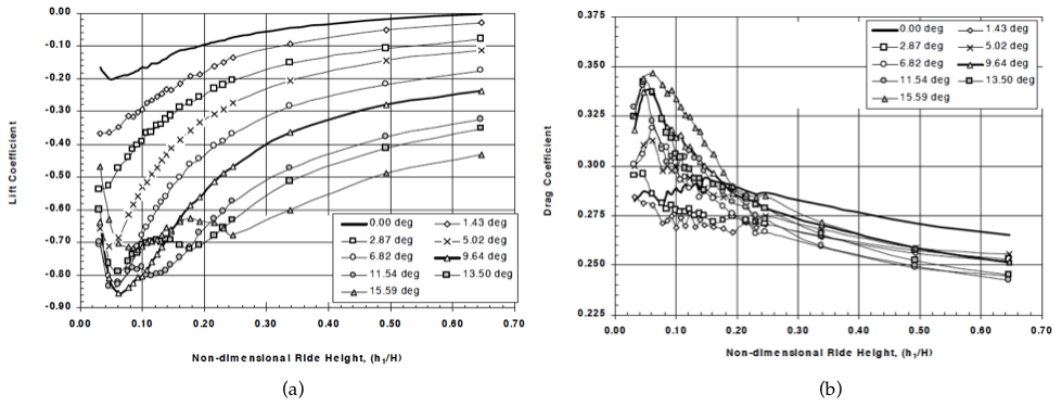

FIGURE 3.6: Measured (a) downforce and (b) drag for short diffuser, moving ground. Extracted from [8]

Regarding the pressure distributions, the plot obtained has the same shape for the different ride heights of the diffuser tested, but with some small differences. The suction peak at the front face of the body increases with decreasing ride height, as well

as the pressure at the underbody and diffuser by increased area ratio due to ride-height reduction. Most of the pressure changes are concentrated near the diffuser inlet due to increasing diffuser pressure recovery as diffuser angle is increased. At large ride heights, a peak in the C_p appears at the leading-edge of the flat underbody. This occurs due to a probable presence of a small laminar separation bubble in the adverse pressure gradient. When the ride height is decreased, this separation bubble disappears as the pressure gradient is reduced by ground proximity. Pressure recovery increases as θ increases and ride height decreases.

As a preliminary conclusion of these wind-tunnel tests, Cooper et al. state that the area ratio AR determines the upper limit of the diffuser pressure recovery, whereas the non-dimensional length (N/L) of the diffuser determines the rate of pressure recovery, hence defining the adverse pressure gradient in the diffuser. For any area ratio, it is obtained that the pressure gradient increases with decreasing non-dimensional length. As mentioned at the beginning of the Chapter 3, the stall of the diffuser will occur if the adverse pressure gradient is higher than that which the boundary layer of the diffuser walls can stand. If this situation occurs the boundary layers will separate from the diffuser walls, reducing the pressure recovery and, hence the diffuser effectiveness. Along with these experimental analysis, Cooper et Al. [8] performed numerical analysis with CFD simulations of the aerodynamic behaviour of diffusers to verify the data obtained on experimental tests, where a maximum downforce was obtained at a larger angle than the indicated by experimental results.

3.4 Numerical Research

A numerical simulation of the Ahmed body geometry with OpenFoam is performed in [16]. The geometry studied has some difference in its dimensions compared to the the normalized Ahmed body geometry: L=1257 mm, W= 300 mm and H = 309 mm. The diffuser length is of 514.5 mm (41% of the total body length) with a slant angle of 17°. The free stream velocity is of 20 m/s. The steady-state solver simpleFoam was applied along with the turbulent model SST and SA. It is obtained that model SST over-predicts the lift coefficient on the model compared to SA, as shown in Fig. 3.7. The main objective of this simulation is observing the vortex generated within flow behaviour across the length of the Ahmed body – see Sec. 3.7 for more information about the generation of vortex.

The results show the presence of a vortex core that rotates in the clockwise direction and a smaller counter-clockwise vortex. This vortex core size increases as closer to ground proximity is the diffuser. From the results obtained, it is concluded that when ride height is decreased, there is:

- Increase in vortex core size.
- Decrease in peak vorticity magnitude.
- Increase in C_L, thus increasing circulation.

In [14], another CFD simulation of the Ahmed body geometry is performed. The dimensions of the model used also differs from the normalized Ahmed body dimensions with the following values: L = 520 mm, W = 200 mm and H = 145 mm. This difference is due to the simulation done in this paper is for validating the results obtained in a wind tunnel test of this model by [21], hence the geometry may

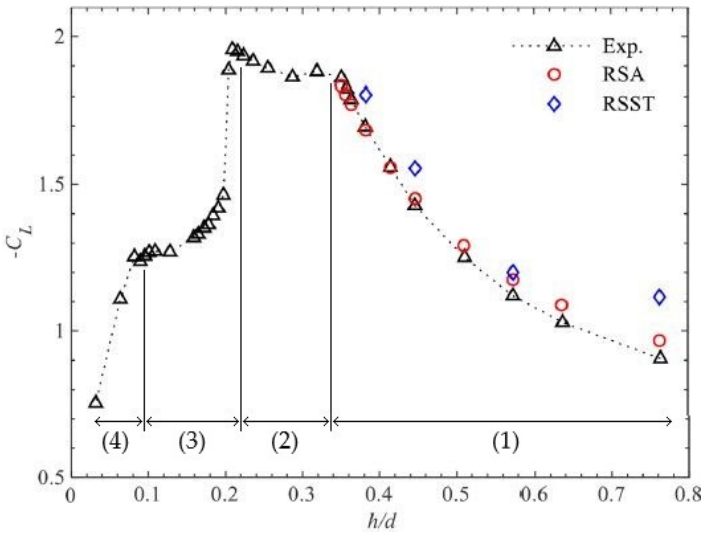

FIGURE 3.7: Downforce coefficient $-C_l$ vs. non-dimensional ride height compared to experimental results of [28]. Extracted from [16]

be smaller due to wind tunnel capacity. The diffuser lengths studied are of 10% and 35% of the total body length. The free stream velocity is of 20 m/s. The aim of this simulation is observing the relationship between ride height and slant angle. For this reason, the range of diffuser angle of 5-35°, with increments of 5°, and a range of ride height between 5-50 mm, 5 mm to 10 mm and from this value the increment of ride height is of 10 mm. The steady-state solver simpleFoam was applied along with the turbulent model k-ω SST with a turbulence intensity of 1%.

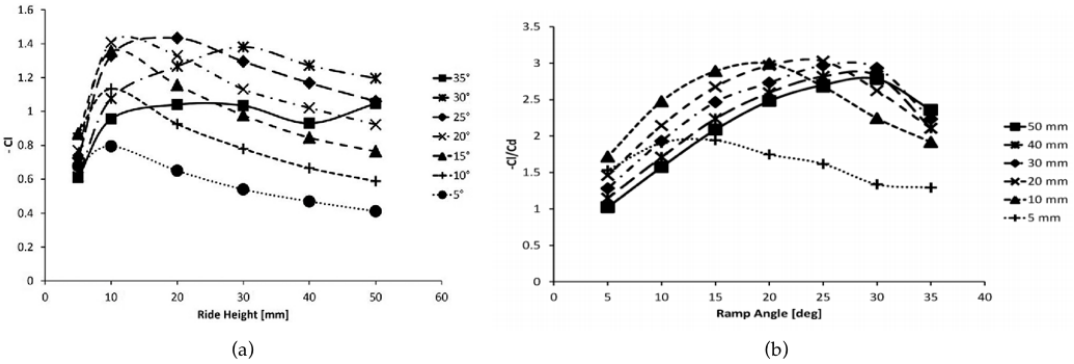

FIGURE 3.8: (a) Downforce coefficient $-C_l$ vs. ride height for different slant angles of long diffuser and (b) aerodynamic efficiency $-C_l/C_d$ vs. slant angle for different ride heights for long diffuser. Extracted from [14]

Once the simulations are performed, results are presented in Fig. 3.8 are obtained. In Fig. 3.8 (a) it is observed that the typical trend of the downforce is increasing from a ride height of 5 mm until reaching a maximum for a ride height of approximately 10 mm, then when increasing further the ride height $-C_l$ decreases considerably. For slant angles of 25°, 30° and 35°, downforce doesn't follow this trend. The 35° diffuser differs significantly from all the other plots as the downforce present little change for ride heights above 10 mm and its maximum occur at the maximum ride height of 50 mm. The maximum downforce is given by the 25° diffuser at a ride height of 20 mm. Regarding the plot of Fig. 3.8 (b), it presents the aerodynamics efficiency

$-\frac{C_l}{C_d}$ against the ramp or slant angle for different ride heights. The aerodynamics efficiency shows the relationship between downforce and drag, hence the bigger this ratio the greater downforce is generated compared to the drag produced. It is crearly seen that the worst ride height is of 5 mm as its maximum value of $-\frac{C_l}{C_d}$ is of 2 approximately with the 10° diffuser. Whereas ride heights of 10 mm and 20 mm present maximum values of aerodynamic efficiency. For a ride height of 10 mm, the optimum configuration was with a 20° diffuser and for 20 mm, 25° diffuser gives optimum performance. From these plots, it is extracted that there is a clear dependency of the ride height and diffuser angle when generating downforce on a body. Finally, it is concluded that if the ride height is increases, the diffuser angle has to be higher in order to maintain optimal efficiency. Values for short diffuser result smaller than for the long diffuser.

3.5 Performance: Downforce

Downforce is the force of lift acting downwards generated on the car. On most street cars, this force helps reducing fuel-consumption and improve the effectiveness of car rides. However, in Formula 1 cars the generation of downforce is taken to the next level, as it enables the car to go on very high speeds while taking corners on a track. It is an important aspect to consider as this force makes sure that the four wheels are always in contact with the track asphalt enhancing the ground grip, thus avoiding problems of stability of the car which could make the car go off the track and lead to a possible accident. This force is created with the aerodynamics of the vehicle. There are several components in a Formula 1 car for downforce generation: front wing, rear wing, underbody and diffuser. Nevertheless, as the subject of study is Formula 1 diffusers, this paper is focusing on how these elements take part on the generation of downforce. [11] Formula 1 aerodynamicists work very hard on designing the different elements of a Formula 1 to generate the sufficient downforce so as to have the maximum performance of the car and prevent accidents while going at high speed. The amount of downforce needed depends on the track which is being driven on: tracks with more corners will need a high downforce so take these corners with a higher speed without slipping, while on tracks with few corners and most straights downforce is needed but in a less proportion. [1]

In [7], the Eq. 3.2 for obtaining the lift coefficient C_L is exposed. Hence, to obtain the optimum and necessary value C_L, in this case negative lift or downforce, the difference between $\overline{C}_{p_l}$ and $\overline{C}_{p_u}$ must be managed the optimum way so as to obtain the desired downforce on the body.

$$C_L = \frac{L}{H}\left[\overline{C}_{p_l} - \overline{C}_{p_u}\right] \tag{3.2}$$

Where L and H are the length and the height of the body, respectively – parameters indicated in Fig. 3.5. $\overline{C}_{p_l}$ and $\overline{C}_{p_u}$ are the lower and upper surface mean-effective pressure coefficients and are obtained from the integral of $C_p(x)$ from 0 to x_i, where i is l or u. In [7], the upper surface mean-effective pressure coefficient $\overline{C}_{p_u}$ is considered as usually constant as it is atmospheric pressure and any changes in geometry happen on the upper surface, therefore C_L will be determined by the lower surface mean-effective pressure coefficient $\overline{C}_{p_l}$. For this reason, the downforce will be maximised by making $\overline{C}_{p_l}$ as negative as possible, as the downforce is the negative lift. The coefficient $\overline{C}_{p_l}$ itself and which elements influence its value must be studied to

know how to maximise this downforce. This lower surface mean-effective pressure coefficient is approximated to the sum of two pressure coefficient components, as shown in Eq. 3.3 [7],

$$\overline{C}_{p_l} = \left(1 - \frac{N}{L}\right)\overline{C}_{p_f} + \left(\frac{N}{L}\right)\overline{C}_{p_d} \tag{3.3}$$

Where N and L are the length of the diffuser and the body (as shown in Fig. 3.5), and the subscripts f and d denote the flat-underbody surface and the diffuser length, respectively. On one hand, the $\overline{C}_{p_d}$ is defined in Eq. 3.4, and depends on C_{p2} and $\overline{C}_p$, which can be obtained from Eq. 3.5 and 3.6. Hence, the diffuser mean-effective pressure coefficient $\overline{C}_{p_d}$ depends on the outlet conditions and overall pressure-recovery coefficient $\overline{C}_p$ (Eq. 3.5).

$$\overline{C}_{p_d} = 1 - \frac{1 - C_{p2}}{\sqrt{1 - \overline{C}_p}} \tag{3.4}$$

The pressure coefficient is the relation between the pressure and the inertial forces of the fluid, as defines Eq. 3.5.

$$C_{pi} = \frac{p_i - p_\infty}{\frac{1}{2}\rho U_\infty^2} \tag{3.5}$$

Where p_i is the static pressure at a point i where the pressure coefficient is being calculated, p_∞ is the free-stream fluid pressure and the term $(1/2)\rho U_\infty^2$ represents the free-stream fluid dynamic pressure from Bernoulli's equation – see Sec. 2.5.3.

$$\overline{C}_p = \frac{C_{p2} - C_{p1}}{1 - C_{p1}} \tag{3.6}$$

Nevertheless, in [7] it is exposed that the determination of a general analytical expression for flat-underbody mean-effective pressure coefficient is not possible. For this reason, in the study a relation between the $\overline{C}_{p_d}$ and $\overline{C}_{p_f}$ is found in order to put the coefficient $\overline{C}_{p_f}$ as function of $\overline{C}_p$ with Eq. 3.4. This relationship between $\overline{C}_{p_d}$ and $\overline{C}_{p_f}$ is obtained in [7] with the numerical integration of the underbody pressure distribution obtained from the CFD simulations performed. The $\overline{C}_{p_f}/\overline{C}_{p_d}$ vs. N/L is plotted and the equation of the curve is obtained: $\overline{C}_{p_f}/\overline{C}_{p_d} = 1.02 + 3.61 \cdot N/L$. It is important to keep in mind that this relation is obtained for non-dimensional parameters, it could be generalised for diffusers of all combinations of ride height and area ratio. Substituting this relation into Eq. 3.3, the following Eq. 3.7 is obtained,

$$\overline{C}_{p_l} = \left[1.02 + 3.59\frac{N}{L} - 3.61\left(\frac{N}{L}\right)^2\right] \cdot \left[1 - \frac{1.19}{\sqrt{1 - \overline{C}_p}}\right] \tag{3.7}$$

This expression relates the lower surface mean-effective pressure coefficient $\overline{C}_{p_l}$ with geometrical parameter of the diffuser N/L and pressure recovery coefficient $\overline{C}_p$. Optimum diffuser design from previous expression is discussed in Sec. 3.6.

3.5.1 Downforce generation mechanisms

In [8], Cooper et al. identified the appearance of 3 fluid-mechanical mechanisms when studying diffuser flow behaviour which are responsible of the generation of downforce on diffusers.

Considering a symmetric Ahmed body — without a diffuser— located far from the ground in free air, no lift is generated on the body as there is no pressure difference from the upper and lower surfaces, as airflow has the same velocity over both surfaces. When approaching the body to ground proximity, airflow beneath the body suffers an increase on its acceleration due to ground constraint — non-slip condition. This phenomenon is called **ground interaction**. The amount of airflow enters the underbody through a smaller inlet area compared to when located in free air. This decrease in the inlet area, as defined in the Venturi effect, makes that the same amount of airflow that in free air entered the bottom surface, now has to flow through a smaller area, thus increasing its velocity to flow through this surface in the same time as did in free air where the inlet area was larger. Due to the increase of flow acceleration beneath the body, this airflow becomes more asymmetrical around the body as on the upper surface the airflow has a certain velocity and on the lower surface it has higher velocity. As stated in Chapter 2, lift generation happens when a body suffers a pressure differential between its upper and lower surfaces — as seen in wing's airflow behaviour. Therefore, as Bernoulli's principle states, this flow acceleration implies a reduction of the underbody static pressure which generates downforce. The smaller the static pressure on the lower surface, the greater the downforce generated as the pressure difference between the upper (atmospheric pressure) and lower surface will be greater. As closer to the ground, airflow acceleration beneath the body increases due to ground constraint reducing the underbody static pressure further, thus generating greater downforce. As in ground interaction mechanism the pressure is reduced from the front-surface suction peak results in a concave plot in the pressure coefficient graph, as shown in Fig. 3.10. Nevertheless, the increase in downforce with ride height decrease is limited due to effects of fluid viscosity. These viscous effects are not prevailing at larger ride heights, for this reason downforce is maximum at a certain low ride height, but if lowered further underbody flow resistance increases due to viscous effects limiting maximum downforce, see in Fig. 3.9 how C_L stops increasing when ride height is close to 0. If lowered enough, flow viscous effects from boundary layer on the lower surface become more significant, leading to *blockage area*, a blocked-area fraction of an internal flow. This phenomenon occurs due to non-uniform velocity profile across the diffuser inlet which becomes increasingly distorted as flow experiences positive pressure gradient. Viscous effects cause an increase of blockage area due to the increase of wall boundary layers with velocity profiles occupy largest fraction of flow cross-section. This distorted velocity profile surely blocks part of the flow cross-section, which reduces the area ratio of the diffuser. The velocity profile non-uniformity is also accentuated by an inviscid mechanism. By Bernoulli's equation, change in static pressure and velocity along an incompressible flow streamtube is defined by Eq. 3.8

$$du = -\left(\frac{dp}{\rho u}\right) \tag{3.8}$$

In the case of a diffuser, change in static pressure is positive $dp > 0$ and velocity reduces $du < 0$. This velocity reduction is highest when the local velocity u is the

smallest, which makes velocity differences across the diffuser more significant and the velocity profile gets highly distorted, leading to blockage. This results in a decrease of the pressure rise, thus reducing the downforce generated. Consequently, it is a phenomenon to bear in mind since it reduces the diffuser performance and effectiveness excessively. [8]

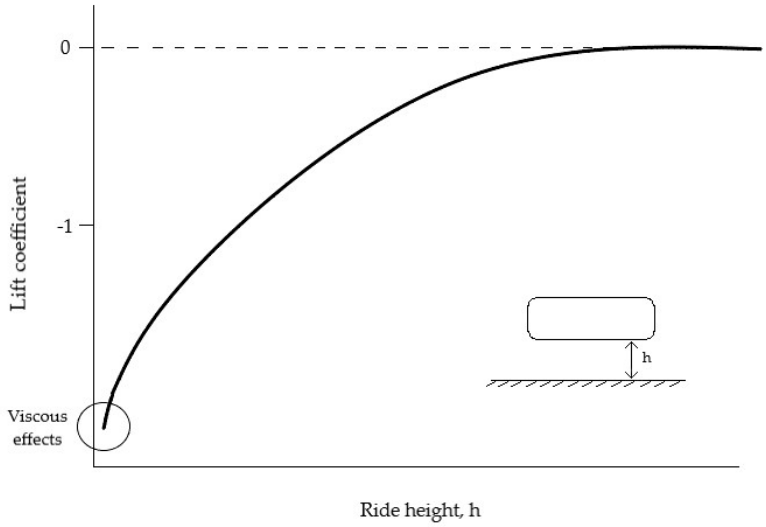

FIGURE 3.9: Variation of lift coefficient with ride height

Even though a body with a flat underbody can generate downforce in ground proximity, the presence of an **underbody upsweep** zone at the rear of a symmetrical body – see Fig. 3.10 – creates cambered shape, resulting in a significant increase of downforce even for large ride heights. The main objective of this mechanism is obtaining a flow asymmetry on the body, as seen for ground interaction but can be obtained at larger ride heigts. When the airflow encounters the upsweep or diffuser with a certain slant angle, it has to change its direction to follow the ramp of the diffuser. This change in the flow direction requires a resultant pressure force that changes the pressure distribution in the lower surface and this phenomenon is responsible of additional downforce generated. A suction peak appears at the inlet of the diffuser, as shown in Fig. 3.10, to prevent flow separation on the ramp of the diffuser. An additional advantage of this mechanism is its effectiveness in reducing drag far from ground. This effect is observed experimentally at the greatest ride height where the body is out of ground effect. Furthermore, the upsweep of the diffuser reorientates upward the counter-rotating streamwise vortex pair, generated by the pressure difference between the diffuser and the region outside its longitudinal sides. These vortices will be discussed in Sec. 3.7. [11]

As introduced in this chapter, the diffuser reintegrates the airflow beneath the body to atmospheric pressure (called base pressure) at the diffuser exit, thus the difference of pressure between underneath the body and this base pressure determines the pressure recovery of the diffuser. The higher this pressure recovery, the greater the downforce produced on the body. The addition of a diffuser reduces the underbody pressure further and, consequently, has greater underbody flow rate and greater downforce. Diffuser can be considered to have *pumped down* the underbody with the increase in the underbody flow rate. Hence, this mechanism is called **diffuser pumping**. It occurs due to the increasing cross-sectional area in the flow direction, which makes a decrease in the flow velocity over the diffuser length from

inlet to outlet with its corresponding increase in static pressure (until reaching base pressure). The relaxation process consisting on delivering the airflow from the underbody to atmospheric conditions as smooth as possible (see diffuser part on Fig. 3.10) requires an outlet to expand it. The bigger this outlet area, the smoother the airflow is delivered to the base pressure. However, as the body is closer to ground, the outlet cross-sectional area is reduced. Thereby, there is a clear trade-off of ground interaction and underbody upsweep mechanisms which depends on the ride height. From Fig. 3.10, it can be extracted that the smaller the pressure coefficient at the diffuser inlet C_{p_1}, as base pressure C_{p_2} is supposed constant, the higher the pressure recovery will be, improving the effectiveness of the diffuser. The main objective of this mechanism is to increase the amount of flow through the underbody flow path, resulting in additional lift components. The more flow beneath the body, the greater downforce generated. However, an additional drag component is also generated by this augmented flow and at small ride heights it can totally cancel the underbody upsweep advantage of reducing drag. Pressure rise is a function of the ratio of the areas at the outlet and the inlet of the diffuser (AR) and the non-dimensional length (N/h_1).

	Ground interaction	**Underbody upsweep**	**Diffuser pumping**
Ride height	Small	Large	Small
Downforce	++	+	++
Drag-reducing	-	+	-

TABLE 3.1: Table with the advantages and disadvantages of each downforce mechanism. Where (++) means it is highly positive, (+) it affects positively and (-) it affects negatively

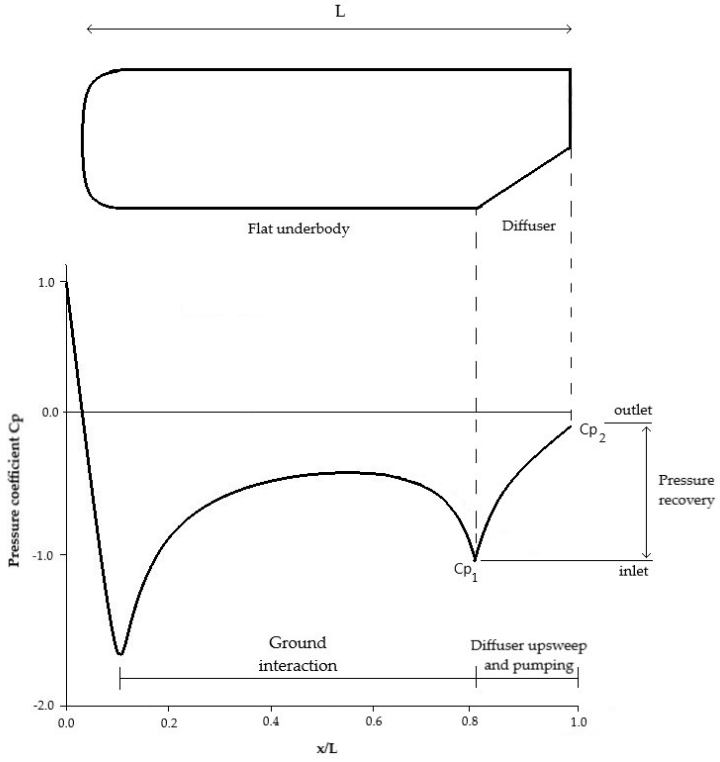

FIGURE 3.10: Representation of the 3 downforce mechanisms in a pressure coefficient plot of an Ahmed body with diffuser

The effectiveness of diffusers is given by the amount of airflow entering into these diffusers. This way, the greater the amount of airflow going into the diffuser, the greater the downforce that will be generated on the vehicle. The diffuser is defined as ride-height and Reynolds number sensitive based on the generation of downforce, in other words, a change in the ride height of in the Reynolds number can suppose a significant change in downforce. The peak of performance is obtained at low ride heights. Additionally, high angles of the diffuser work better with high ride heights, whilst, on the contrary, low angles perform better with low ride heights.

In summary, it is important to understand these 3 mechanisms and how they affect each other in order to determine the optimum diffuser geometry. First, ground interaction and diffuser pumping provide an increasing amount of downforce, while the upsweep angle reduces the drag considerably. Low ride heights are advantageous for downforce generation in ground interaction and diffuser pumping, which cancels the reduction of drag of the underbody upsweep. For this reason, it is stated that there is an obvious dowforce/drag trade-off which depends on the ride height of the diffuser (see Tab. 3.1). Consequently, the ride height must be chosen consciously depending on the necessities: if drag-reducing is important, larger ride heights will be implemented and if downforce generation is more significant, then smaller ride heights will be used considering the drag penalty.

On the other hand, in [28] the plot of the downforce coefficient $-C_l$ against the ride height is divided into 4 different regions characterizing the downforce behaviour of ground-effect diffuser. In Fig. 3.7 presented in Sec. 3.4 these 4 regions are clearly defined. [16]

1. **Force enhancement**. Downforce increases with decreasing ride height. A symmetric pair of counter-rotating vortices with a high axial-speed core and high levels of vorticity are present in the diffuser at this region.
2. **Force plateau**. If ride height is decreased, downforce stabilizes on the upper limit of the plot in a linear approximation. The diffuser flow remains symmetric, however, the vortices significantly increase in size and the vortex cores has low axial speeds. At this region, ride height reaches a critical value.
3. **Force reduction**. In this stage, with further ride height reduction downforce considerably decreases. The symmetric vortex flow within the diffuser breaks down and results in a separated asymmetric flow through the diffuser.
4. **Loss of downforce**. As the name states, if ride height is decreased reaching extreme small values, near 0 mm, the generation of downforce is stopped. What happens is that the flow within the diffuser is totally blocked due to viscous effects for being so close to ground proximity and, hence airflow cannot go through. As defined for ground interaction mechanism, the phenomenon of blockage area occurs. This results in a separated asymmetric flow appearance.

3.6 Geometry

In [7], the experimental and numerical studies done in [8] are analysed to obtain a generalised method to define optimum diffuser geometries. In this paper, an analytical model of the diffuser is obtained so as to determine these optimum diffuser geometries. By examining the diffuser performance of the downforce generation, the optimum diffuser design parameters are obtained. Eq. 3.9 is obtained to make

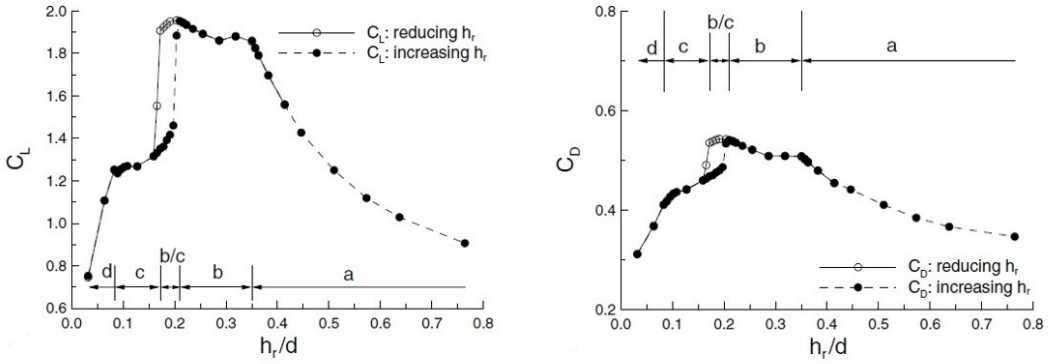

(a) (b)

FIGURE 3.11: Representation of the 4 regions in (a) downforce and (b) drag coefficients with the phenomenon of hysteresis. Extracted from [28]

a relation between the diffuser design parameters (area ratio, ride height and length of the diffuser), hence this formula can be used to determine the parameters when designing a diffuser.

$$AR = 1 + \frac{N}{h} tan\theta \tag{3.9}$$

Where N is the diffuser length, h the ride height and θ the diffuser slant angle. Vehicles with a greater ride height imply smaller area ratio for a given diffuser slant angle compared to that of a lower ride height. [20] If ride height h increases or diffuser angle θ decreases, the area ratio AR increases. In [7], it is exposed that in order to have the internal flow approach 2D flow, aspect ratios of about 10 are used. Downforce increases when area ratio is increased until reaching a value of $(AR - 1) = 2.02$ and then decreases for larger area ratios.

Otherwise, in Sec. 3.5 the Eq. 3.7 is exposed from which the non-dimensional length of the diffuser can be obtained solving that equation. One possible benefit of the curved diffuser is that any local flow separation and reattachment could give locally reduced skin friction and consequently reduce the generation of drag. [11]

One of the conclusions extracted from [7] is that the **best diffuser length** is of the order of **one half the length** of the body or less. Hence, it is concluded that larger diffuser do not imply greater downforce.

The different flow phases on a bluff-body diffuser with their corresponding change in performance suffered is exposed for several ride heights. At large ride heights, when ground interaction is not significant, a vortex rolls up on each side of the floor of the body. These vortices take air with high energy from outside the body into the diffuser. With a reduction in the ride height, the airflow in this conditions tends to create a separation bubble. However, downforce is not disturbed and continues to increase even though the appearance of the bubble. The flow is not in a totally steady state, moving still relatively stable. [27]

Once a critical level is reached the higher angle diffusers achieve the same downforce (at different heights). What's interesting is that the highest angle tested has the largest ride height range at max performance.

If a body (or a large part of one) has substantial ground clearance then the chances are that there is air below that body which is relatively undisturbed. If true, then the higher the body, the more air is sitting there not being used. Conventional flow expansion in two dimensions is not going to take advantage of that energy.

3.6.1 Effects of diffuser length

The optimum non-dimensional length of the diffuser N/L can be determined with Eq. 3.3, Eq. 3.6 and Eq. 3.7 of the analytical model described in Sec. 3.5 [7]. From Eq. 3.3, the parameter N/L makes $\left(1-\frac{N}{L}\right)$ and $\left(\frac{N}{L}\right)$ determine which pressure coefficient $\overline{C}_{p_f}$ and $\overline{C}_{p_d}$ is a greater contributor to the lower surface mean-effective pressure coefficient. For small values of N/L the flat component is more negative than the diffuser's because $\left(1-\frac{N}{L}\right)$ is greater than $\left(\frac{N}{L}\right)$. The flat component becomes more negative by the following expression,

$$\overline{C}_{p_f}/\overline{C}_{p_d} = 1.02 + 3.61(N/L) \tag{3.10}$$

But the parameter that multiplies it $\left(1-\frac{N}{L}\right)$ makes its contribution to $\overline{C}_{p_l}$ reduces. Regarding the diffuser component, as defined in Eq. 3.4, as higher the value of $\overline{C}_p$, greater will be the diffuser coefficient and its weight thanks to $\left(\frac{N}{L}\right)$ increases as the diffuser length increases. At a certain diffuser length, $\overline{C}_{p_l}$ reaches a maximum and then decreases with fur- ther increase of the diffuser's length, and the opposing effects in the flat component continue. In the paper [7], $\overline{C}_p$ reaches a maximum when $\left(\frac{N}{L}\right) = 0.31$. Past this maximum value, $\overline{C}_p$ decreases and $\overline{C}_{p_d}$ increases, being less negative which implies a drawback for downforce generation. Moreover, $\overline{C}_{p_f}$ becomes more negative considering Eq. 3.10 which makes $\overline{C}_{p_l}$ become more negative even for larger values of diffuser length past the maximum and hence increasing downforce. However, if $\left(\frac{N}{L}\right)$ is further increased, $\overline{C}_{p_d}$ becomes less negative making $\overline{C}_{p_l}$ increase, reducing downforce.

3.6.2 Effects of ride height

The ride height is defined as the distance from the flat underbody to the ground. As the diffuser ride height is gradually lowered, the flow behavior within the diffuser changes from attached to separated and this influences the aerodynamic performance of the diffuser. How ride height influences downforce generation is clearly observed in the plot of Fig. 3.11 (a) where 4 differentiated regions are determined. For force enhancement region, as ride height is lowered downforce increases significantly. Then if further ride height reduction, it reaches a critical value with maximum downforce acting on the body. On intermediate region b-c, between force plateau (region b) and force reduction (region c), aerodynamic hysteresis occurs. This phenomenon is explained in Sec. 3.7. If more ride height reduction is applied below this critical value, region c and d take action with a substantial downforce reduction. As the ride height of the diffuser was reduced toward its maximum-downforce height, downforce enhancement was accompanied by increasing suction at the diffuser inlet, enhancement of streamwise flow velocity and low pressure along the lengthwise sides of the diffuser due to the strengthening of the longitudinal vortices. [11]

Fluid viscosity is of minimal concern for larger ride heights, however this becomes a dominating factor with reduced ride height due to the restricted area underneath the body for which the flow to travel. At very low ride heights, the flow rate under the body is reduced due to the underbody cross-sectional area is choked due to viscous forces are dominant on the boundary layer, thus downforce generated is also restricted. [20]

3.6.3 Effects of diffuser slant angle

The diffuser slant angle θ is the angle between the flat underbody and the line that creates the diffuser (see Fig. 3.5), and affects the effectiveness of the diffuser. If it is too steep, it will cause a separation of flow under the car, and will increase the the effect of turbulence and increase drag. Otherwise, if it is too shallow, it will reduce the ability of the diffuser to create a low-pressure zone at the bottom of the Formula 1 car. However, the diffuser angle also has high influence on the downforce generation of the car. [1]

If the angle of the diffuser is close to zero the boundary layer flow will not detach, but the air speed will not be reduced enough to make a laminar transition of the air at the end of the car when to two airstreams meet. If the diffuser has a very large angle the boundary layer flow will detach and the airflow underneath the diffuser will be turbulent. So the angle of the diffuser is limited: when the angle is too small or too large the diffuser will create more drag then necessary. [13]

3.7 Vortex

As defined in [26], a vortex is a *spinning flow of fluid with closed streamlines*, in which its core is a low pressure zone and this pressure increases progressively with distance from the center. The circular movement of fluid within vortices contains a lot of energy, which if it was an ideal fluid this energy cannot be dissipated and the vortex would never disappear. Nevertheless, regarding real fluids due to their viscosity the energy is dissipated very slowly from the core of the vortex. This high energy can be taken advantage of to prevent flow separation with the help of vortex generators, which delay flow separation even when the critical Reynolds number is exceeded. In a vehicle, the existence of vorticity is produced by viscous shear in the boundary layers in contact to solid surfaces. [26] One of the functions of vortices in a Formula 1 car is to help sealing the lower pressure area under the car to prevent fluid loses through the sides of the car, ensuring **high mass flow rate entering the diffuser**. When these vortices appear, they roll up under the diffuser taking high energy air from the outside of the body and introducing it into the diffuser but they also take high energy air from below the level of the body and mix it into the body of airflow under the diffuser. This phenomenon enables the diffuser to function at high angles without detaching and losing effectiveness. [27]

The presence of a trailing counter-rotating vortex pair in the diffuser should induce some level of upwash. Consequently by Newton's 3rd Law of action-reaction, the downforce acting on the diffuser body is the consequence of the force reacting to the diffuser flow being redirected upwards by the trailing vortex pair [16]. In [28], the authors predict that the circulation of this counter-rotating vortex pair is directly related to the downforce produced.

$$\Gamma = -\int_A \omega \cdot n \, dS \simeq \omega \cdot S \tag{3.11}$$

Where ω is the vorticity and S the surface. Regarding Eq. 3.11, in order to increase the circulation when ride height is decreased – S is decreased–, the vortex size (vorticity) must grow at a faster rate such that their product continues increasing to maintain the circulation. When considering vortex in a diffuser, its size is limited by the diffuser dimensions that decrease with decreasing ride height. The authors postulate that the transition from the force enhancement region to the force plateau region is a result of the trailing vortex pair growing to the size of the diffuser. In the experimental results obtained by Zhang et al. [28], while in the region (2) of force plateau – defined in Sec. 3.5.1– the counter-rotating vortex pair still filled the diffuser. At this point, the vortex core is no longer surrounded by an inviscid flow field and now interacts with the wall boundary layer. This results in a change in the dynamics of the vortex, hence changing lift generation behavior.

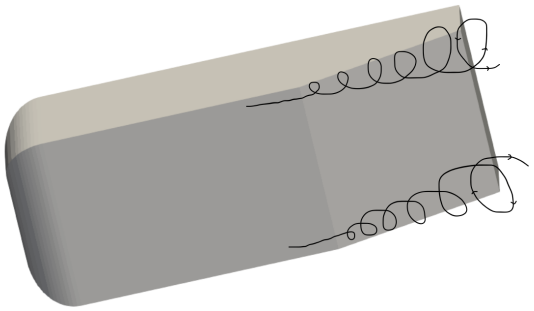

FIGURE 3.12: Pair of vortex formed at the underbody

The presence of vortices and their development within the diffuser highly depends on the region the body is working. If studying the force enhancement region, for larger ride heights – far from ground –, two vortex roll up, one on one side of the underbody and the other on the other side as shown in Fig. 3.12. Both these vortices originate on the corners of the diffuser inlet and expand as they move downstream on the diffuser ramp, moving inboard. These vortices imply the presence of additional high energy air entering the underbody which is pulled in from the outside introducing it into the diffuser. Consequently, a region of negative pressure appears at the diffuser inlet due to this increment of mass flow rate. Besides, greater slant angle increases vortex strength and prevent flow separation at the diffuser ramp. During this region, the flow is symmetrical and is attached on the diffuser ramp (Fig. 3.13 (a)) and if ride height is decreased, downforce increases (see Fig. 3.11 (a)). As the ride height is lowered, the main vortex move further to the interior of the diffuser and their size increase. A highly concentrated vortex core implies stable vortex flow [28]. If ride height is lowered further, a separation bubble appears in the diffuser ramp which provokes a sudden increase of the vortex size after separation (but lose strength), hence downforce continues to increase. This is what happens in the force plateau region b, as can be seen in Fig. 3.11 (a), downforce decreases a little but suddenly suffers an increase reaching its peak at a critical value of ride height; below this the downforce starts decreasing. In this phase, flow is still symmetrical but it is a bit disturbed as shown in Fig. 3.13 (b).

Then force reduction region begins when ride height is further decreased below this

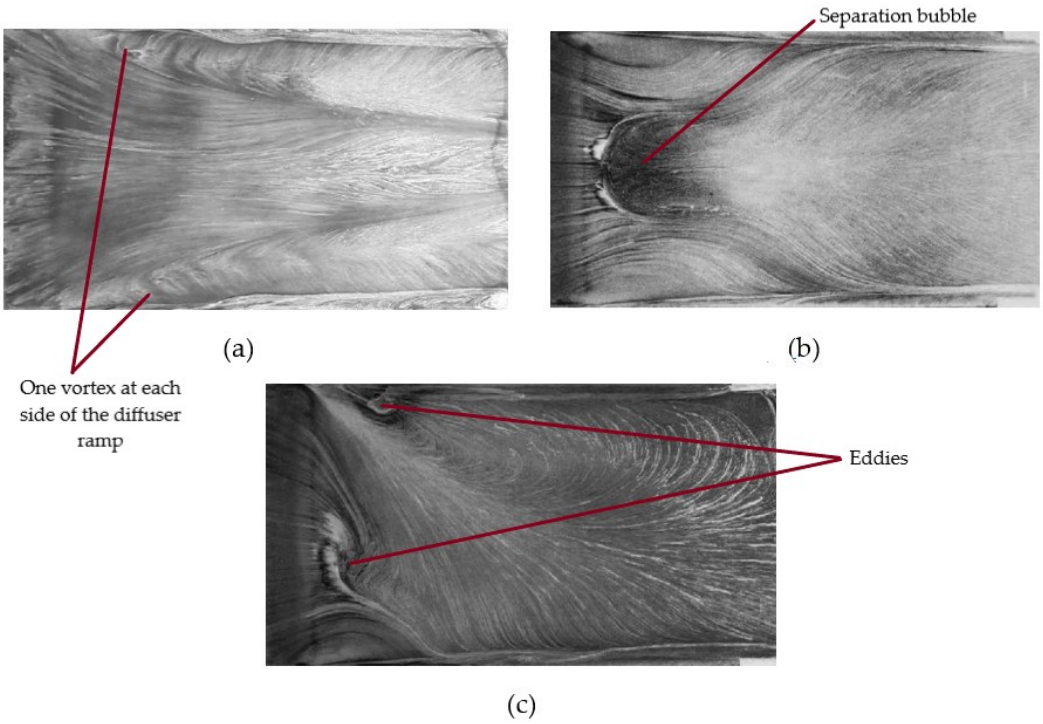

FIGURE 3.13: Flow behaviour in (a) force enhancement, (b) force plateau and (c) force reduction. Extracted from [27]

critical value. From Fig. 3.13 (c), vortex in this phase are clearly asymmetrical with one main vortex dominating the flow behaviour at the diffuser ramp. This occurs because when the ride height is lowered, one of the two vortices burst (the vortex that burst is random) resulting in one main vortex. This provokes a great reduction in downforce as can be seen in region b-c of Fig. 3.11 (a). The rest of the flow enters in a weak re-circulating region with an axial flow reversal due to flow separation at the diffuser inlet. Consequently, a loss of suction occurs confirming the vortex breakdown. In this region, once the vortex has burst, to improve the situation of the flow, ride height must be higher than the ride height at which the vortex burst so as to obtain the symmetrical flow that there was before. As burst and re-creation happen at different heights leads to what it is called aerodynamic *hysteresis*. This is why the plot of downforce and drag in Fig. 3.11 presents two lines between the force plateau and force reduction regions – one for increasing and another for decreasing ride height. Additional ride height reduction implies smaller energy and worsen attachment of the flow, resulting in complete separation on the whole diffuser surface.

4 CFD simulations

In the recent years, the automotive industry has used methods to increase fuel efficiency or decrease pollutants from exhaust gases due to the current interest in environmental issues. For this reason, the wind tunnel has been a great ally to assess vehicle aerodynamic performance, thus improving the efficiency and the performance of cars. Nevertheless, wind tunnel tests are quite expensive and the extraction of results is very time-consuming as well. Here is where Computational Fluid Dynamics (CFD) takes action due to its shorter time period of the vehicle design process and low cost on the experimental measurements compared to wind tunnel tests. In comparison with CFD, wind tunnel experiments are expensive, provide limited information and it is difficult to achieve sufficient turn-over. Otherwise, numerical modeling in CFD is particularly useful in understanding the flow or looking for qualitative improvements, and it is used in five major areas in the automotive industry: vehicle aerodynamics, thermal management (cooling and climate control), cylinder combustion, engine lubrication and exhaust system performance. Moreover, it is widely known that in Formula 1 CFD is mostly used to perform aerodynamic analysis on the different aerodynamic elements in the vehicle for improving the performance of the car to be as fast as possible. A good aerodynamic analysis increases the downforce generated on the car, which improves the adhesion of the vehicle to the ground increasing the cornering speed to improve lap times.

In this section, 3 three-dimensional CFD simulations are performed on an Ahmed body geometry in order to observe the flow behaviour described in Chapter 3. The CFD software used is OpenFOAM© as it is a free open-source software option available to provide numerical solutions to the desired geometry. Beforehand, a familiarization stage with the software was done as presented in Annex A with the simulation of different cases. In Sec. 3.3 and Sec. 3.4 several studies on the Ahmed body flow were exposed. However, as **the study of Knight et al. [14]** about the performance on an Ahmed body is **the most recent** of the researched, it is the one taken as reference to validate the results obtained. The following simulation conditions defined in the article are imposed in the case of study:

- Free-stream velocity: $U_\infty = 20\ m/s$ (72 km/h). Knight et Al. used this velocity on their simulations as it is the velocity used in the wind tunnel tests too, it is supposed that the wind tunnel cannot acquire very high velocities. Furthermore, Formula 1 cars are known for their extremely high velocities. However, these high velocities appear specially on long straights where the gas pedal is fully pressed and there is no need to brake. A velocity of 20 m/s may seem small for a Formula 1 car, but as explained before diffusers are added to create downforce to improve the cornering speed. When cornering, velocities do not reach very high velocities, but small velocities. For this reason, in the simulations this velocity of 20 m/s is introduced as initial velocity.
- Newtonian fluid: $\nu = 1.5 \cdot 10^{-5}\ m^2/s$

- Turbulence model: $k-\omega SST$. In the article [14], Knight et Al. makes a comparison between both RANS turbulence models $k-\varepsilon$ and $k-\omega SST$ and the wind tunnel tests results. It is concluded that the $k-\omega SST$ turbulence model is more accurate than the $k-\varepsilon$. Additionally, $k-\varepsilon$ usually gives worse results on external aerodynamics cases.
- Turbulence intensity I: 1%. This parameter is defined by the ratio between the turbulent velocity fluctuations and the mean velocity. Typically in cases of external aerodynamics, for instance around a vehicle, can be considered as low turbulence case with a very small turbulence intensity of 1% [6].

Additionally, the ride height set for all simulations is 20 mm, as in the article represents one of the optimum ride heights. Even though the numerical simulation of the article [14] the solver used is the steady-state *simpleFoam* (SIMPLE algorithm), the solver to be used in this study is the transient solver *pimpleFoam* (PIMPLE algorithm). This way, the transient solver enables to capture the unsteady state that occurs in the diffuser. As explained in Sec. 3.7, the flow can suffer hysteresis with any flow change, and unluckily steady state solver can not pick that up. Additionally, the time evolution of the vortices can be better observed.

All the cases simulated have the scheme of directories presented below. The bold ones represent the directories inside the case. There are 3 directories. In the directory **0** where the initial conditions are established. Then on the folder **constant** the properties of the fluid and turbulence model are established as well as the geometry in format .stl is found located inside the subdirectory triSurface from where the meshes reads the geometry file. Finally, in the **system** directory, the dictionaries for the mesh generation and the solver conditions are set.

Case	**/0**	U
		p
		k
		ω
		nut
	/constant	**/triSurface**
		transportProperties
		turbulenceProperties
	/system	blockMeshDict
		controlDict
		forceCoeffs
		fvSchemes
		fvSolution
		snappyHexMeshDict
		surfaceFeatureExtract

4.1 Model and solver

External flows are difficult to approximate because it is hard to evaluate the flow downstream taking into account anything that could have affected the turbulence. For these simulations, the $k-\omega SST$ (Shear Stress Transport) RAS turbulence model is used. It consists of a two equation model to approximate the turbulence of the

flow. The corresponding two equations are Eq. 4.1 is the equation that calculates the turbulence specific dissipation rate ω and Eq. 4.2 is the equation for the turbulence kinetic energy k [18].

$$\frac{D(\rho\omega)}{Dt} = \nabla \cdot (\rho D_\omega \nabla\omega) + \frac{\rho\gamma G}{\nu} - \frac{2}{3}\rho\gamma\omega(\nabla \cdot \mathbf{u}) - \rho\beta\omega^2 - \rho(F_1 - 1)CD_{k\omega} + S_\omega \quad (4.1)$$

$$\frac{D(\rho k)}{Dt} = \nabla \cdot (\rho D_k \nabla k) + \rho G - \frac{2}{3}\rho k(\nabla \cdot \mathbf{u}) - \rho\beta^*\omega k + S_k \quad (4.2)$$

The turbulence kinetic energy k and the turbulence specific dissipation rate ω must be calculated so as to initialize the model at the first iteration. The variable k is defined by Eq. 4.3 [12], hence only the reference velocity U and turbulence intensity I must be determined. In this case, the reference velocity is of 20 m/s and the turbulence intensity is considered of 1% as a condition of the simulation. The initial value for the turbulence kinetic energy results in 0.06 m^2/s^2.

$$k = \frac{3}{2}(\mathrm{U}I)^2 \quad (4.3)$$

Moreover, one way of approximating the parameter ω is by approximating the turbulence length scale. Nevertheless, for external flows this parameter is not easy to estimate. For this reason, there is another good technique to approximate the turbulence specific dissipation rate which is by the eddy viscosity ratio μ_t/μ—the ratio between turbulent viscosity and molecular viscosity. By research on different articles and websites, this ratio is estimated to a value of 1, as it is shown it is a good approximation for the type of simulation considering its Reynolds number and the low turbulence. This ratio along with the turbulence kinetic energy and the kinematic viscosity ν are used to determine ω by its definition on Eq. 4.4 [12]. The fluid is considered to be newtonian with a kinematic viscosity of $1.5{\cdot}10^{-5}$ m^2/s.

$$\omega = \frac{k}{\nu}\left(\frac{\mu_t}{\mu}\right)^{-1} \quad (4.4)$$

Considering the values of the corresponding parameters of the previous equation, the turbulence specific dissipation rate has an initial value of 4000 1/s. When the values of k and ω are determined, they must be added each to its own file inside the 0 directory.

Regarding the solver used, almost all articles researched that performed CFD simulations used the steady-state solver with SIMPLE algorithm. However, in this project the the variation with time of the diffuser flow behaviour is desired to be obtained. For this reason, the transient solver *pimpleFoam* will be used to principally observe the development of the vortex generated. To ease convergence, first the command *potentialFoam* is run in order to initialize the velocity field solving for potential velocity. Then, the *simpleFoam* is run to obtain the steady-state solution to later initialize the transient solver *pimpleFoam*. The pimpleFoam is corrected with 3 nCorrectors, 3 nOuterCorrectors and 1 nNonOrthogonalCorrectors. With the use of this correctors at each time step, the number of total iterations can be reduced. The detailled

steady-state and transient solvers conditions, as well as the schemes used for each, are presented in Annex B.3.7 and B.3.8.

4.2 Boundary and initial conditions

As in Sec. 4.4.2, 4.5.2 and 4.6.2 is exposed, the mesher used is *blockMesh* along with *snappyHexMesh*. In *blockMeshDict* the patches of the mesh walls created with the *blockMesh* function are established. The boundary conditions for each wall of the block mesh is represented in Fig. 4.1.

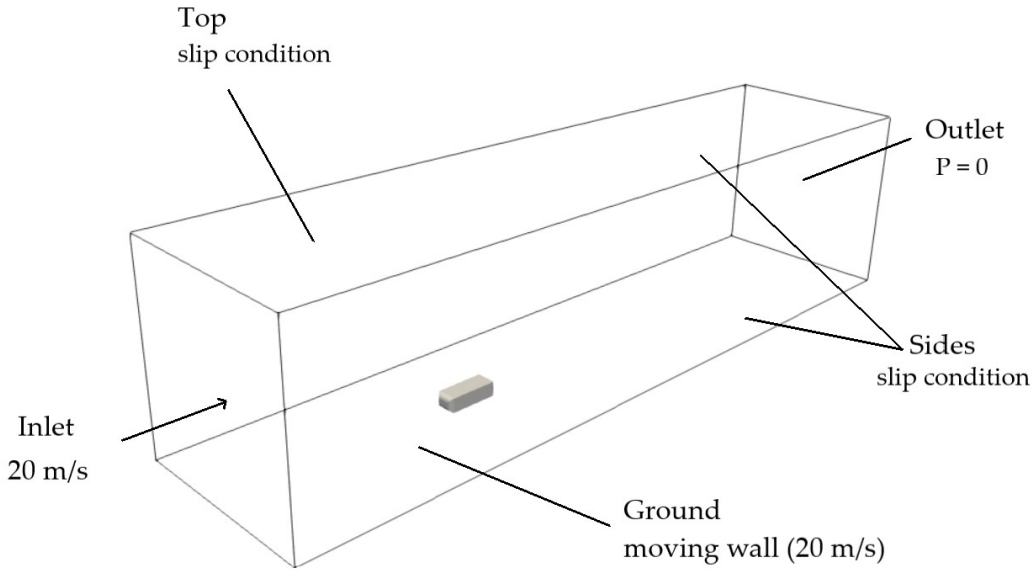

FIGURE 4.1: Representation of the boundary conditions of the mesh

These patches are related to the boundary conditions defined in the *0* directory, as they must be compatible with the boundary and initial conditions of each surface. The initial conditions of the parameters U, p, k, ω and nut must be introduced each on its own file inside the 0 directory of the case in OpenFOAM©. For the wall boundary conditions, wall functions for k, ω and nut are used. Wall functions are equations that describe better the flow near the wall. These wall functions are used because of the very small cell requirements in certain areas of the mesh where boundary layer is dominant, hence it would be required to apply a finer application of the values of these parameters to obtain a more accurate solution. They are used when the computational resources are limited and the number of cells of the mesh can not be as large as needed to obtain a wall distance $y^+ \approx 1$ near the wall. Wall functions are applied on the ground and on the Ahmed body surface, where the boundary layer is important to study the flow behaviour better.

As stated previously in the introduction, in the article [14] it is defined a uniform `internalField` —flux into the domain, the equivalent to a flux into a wind tunnel— with a value of 0 for the pressure and U_∞ of 20 m/s (approximately 72 km/h) in the x-axis (for the rest of axis, the value is 0) for the velocity. Hence, the internal field of velocity U results in (20 0 0). Regarding the inlet and ground, the pressure is constant, so initial condition is set to `type zeroGradient` and velocity is set to `fixedValue` with the value of velocity internal field defined previously. Hence, the ground is considered as a moving wall to simulate the ground condition on a

Formula 1 car. For the outlet, the pressure has a `fixedValue` of 0 and the velocity condition is `type inletOutlet` which is usually acts as condition of `zeroGradient` when the fluid flows out of, it is leaving, the domain, but it switches to `fixedValue` – in this case, the fixed value is defined as `InletValue` – if the fluid is entering the domain (inflow). For sides and top boundaries, both pressure and velocity have slip conditions, which means that the effect of shear stress is considered zero. Finally, for the Ahmed surface —surface corresponding to the geometry of the body studied— it is applied a condition of `type zeroGradient` for pressure and a `fixedValue` of uniform (0 0 0) in all directions for the velocity, in other words, it is prescribed as a non-slip surface.

Regarding the turbulent parameters, the values of k, ω and *nut* are the ones calculated in the previous Sec. 4.1. Boundary *inlet* has `fixedValue` condition on both k and ω and ground has the same initial conditions as in U and p: `type inletOutlet`. However, in either ground and the Ahmed body surface boundaries `kqRWallFunction` and `omegaWallFunction` wall boundary conditions are applied for k and ω, respectively. Finally, for the *nut* initial boundary conditions either inlet, outlet, top and sides are set to `type calculated` with a value of 0, whereas for type wall boundaries ground and Ahmed body surface `nutkWallFunction` wall boundary condition is applied. For sides and top, both have slip conditions as for the pressure and velocity conditions.

In Annex B.1 all the files of directory `/0` containing the values of the boundary and initial conditions are presented.

4.3 Computational set-up

For the realization of the simulations, the laptop used is an ASUS Zenbook UX533F. The main specifications of the computer are the following:

- Operating system: Windows 10 64 bits
- Processor: Intel Core i7 (8th Gen)
- RAM: 16GB
- 1 TB SSD

Hence, neither supercomputer nor a cluster is used to perform all the simulations. For this reason, the number of cells of the meshes can't be very high due to the lack of computational resources.

4.4 Ahmed body with $\theta = 0^\circ$ diffuser

The first case of study is an Ahmed body without a diffuser, hence with a slant angle of 0°. The ride height selected for all cases is 20 mm, as stated previously. In [14], there is no lift and drag coefficient value for a 0° diffuser configuration as the minimum slant angle tested is of 5°. Hence, the results obtained will be validated considering the diffuser configuration with the smallest slant angle at 20 mm ride height in Fig. 3.8, knowing that the downforce for 0° should be smaller. Then this case will be compared with the configuration presented in Sec. 4.5 incorporating a

diffuser at the rear of the body. The comparison between these two cases is interesting since it will be observed how the addition of a diffuser improves substantially the generation of downforce compared to the same body that didn't incorporate one.

4.4.1 Geometry

The geometry used for this simulation is the Ahmed body without a diffuser at the bottom rear, as shown in Fig. 4.2. The dimensions of the body are the ones presented in [14], which are a half of the dimensions of the standardized Ahmed body (see Sec. 3.2). This reduction in the dimensions of the Ahmed body is due to in the article, the CFD simulations done are compared with experimental tests done in wind tunnel, in which the geometry with the standardized measurements can not be fitted. A drawing with the dimensions is presented in Fig. 4.15.

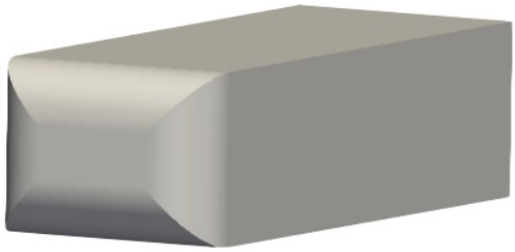

FIGURE 4.2: Dimensions of the Ahmed body geometry used

For the meshing process, it is important to refine the sharp edges, specially the ones at the outlet of the flat underbody in order to obtain accurate results on the airflow leaving the underbody.

4.4.2 Meshing

The mesh is made first with *blockMesh* and then *snappyHexMesh*. The dimensions of fluid volume surrounding the body are 8mx2mx2m, leaving only a distance between the ground and the Ahmed body of 20 mm. On the first place, the start mesh is created running the *blockMesh* command. The block configuration on each axis defined in *blockMeshDict* (see Annex B.3.1) is (40 15 10), as shown in Fig. 4.3. No compression is applied to any axis, since *snappyHexMesh* does not support well this compression in its meshing process.

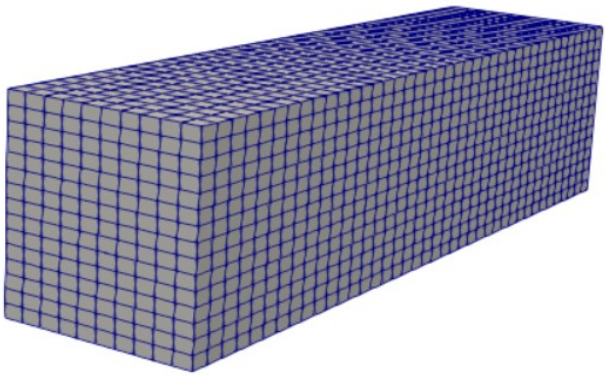

FIGURE 4.3: Initial block mesh done with *blockMesh*

Once the base mesh is done, the function *surfaceFeatureExtract* is run in order to extract the edge features of the geometry (in format .stl) and save it to a new file named *ahmed.eMesh* located in the constant/triSurface subdirectory. This is useful to define the edges so later the *snappyHexMesh* can refine these zones of the geometry more accurately. The following step is defining the conditions of the *snappyHexMesh* mesh inside the *snappyHexMeshDict*. This mesher has the possibility of enabling 3 steps: castellatedMesh, snap and addLayers. These three functions are enabled in the meshing process of the case. However, first of all the geometry desired to mesh is selected and indicated to the mesher. Additionally, three refinement boxes are defined:

- Refinement Box. The first refinement box defined is bigger that the other two. It contains the whole Ahmed body, as well as the other two refinement boxes. It concentrates the cells closer to the flow acting on the body.
- Refinement Ground. As the body is lowered to a very small value of ride height (20 mm), the zone between the ground and the bottom Ahmed body surface must be refined to improve the results calculation so as to consider the effect of the boundary layer in this zone.
- Refinement Wake. This refinement box is created with the aim of defining better the flow around the body, specially the one leaving the diffuser outlet, the wake formed in the rear part of the body.

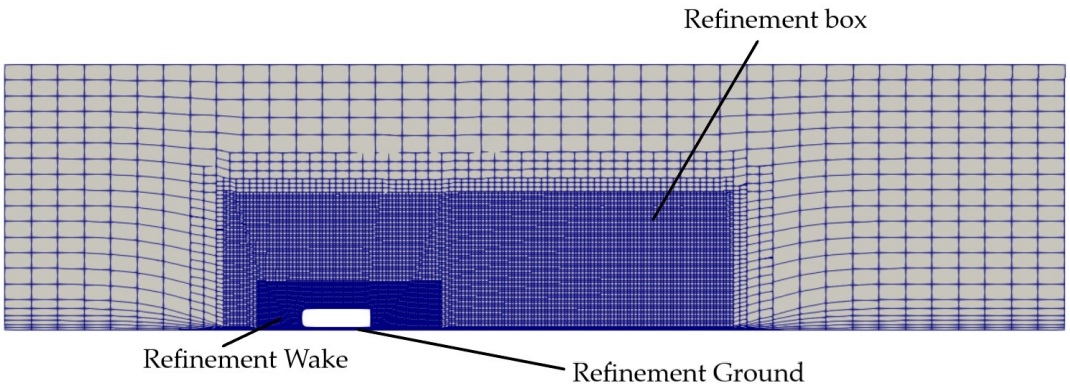

FIGURE 4.4: Side view of the mesh of the Ahmed body with 0° diffuser configuration

In the castellatedMesh part, the mesh close to the features and the geometry surface are refined so as to make easier the snapping phase. The edge features are extracted from the *edgeMesh* containing the features from the tri-surface file (.stl file) obtained from the previous *surfaceFeatureExtract* function. The level of refinement of these features are set to 5, rather high value to apply a good refinement on critical zones as are the edges on the Ahmed body geometry. Also, the level of surface refinement is established to a minimum of 5 and a maximum of 6 on the whole Ahmed surface. Regarding the refinement regions defined previously, the refinement box is refined with a level (3 3), whereas the ground and wake refinement regions are set to (3 4) level of refinement, in order to concentrate the cell on these zones where flow presence is more significant. Then, the snapping phase has the aim of adapting the castellated mesh to conform to the geometry. And finally, cell layers are inserted in the proximity of the body surface and the ground. The number of layers established

are 6. All these parameters defined can be seen in the *snappyHexMeshDict* in Annex B.3.3.

After making sure all the mesher conditions were correct, *snappyHexMesh* command is run and the final mesh observed with ParaView is shown in Fig. 4.4. The blocks of the mesh done with *blockMesh* can be seen with the refinement regions defined in the *snappyHexMesh* inside surrounding the Ahmed body. As closer to the geometry, the cells become more concentrated around the surface. Additionally, as a refinement region was created for the ground closer to the surface, there a concentration of cells in this bottom of the mesh, on the underbody of the geometry.

Looking closer to the Ahmed body and ground proximity, the layer addition can be observed – see Fig. 4.5. This cells concentrated and shrunk closer to the walls will enable the better study of the flow in these zones. It is very important to add layers around the geometry of the Ahmed body, as well as over the ground. These two regions are the most critical as it is where the boundary layer develops and where has more effect. The better it is describe the effect of this boundary layer in this regions, the better results can be obtained. If this mesh phase wasn't done, the results obtained will be distorted.

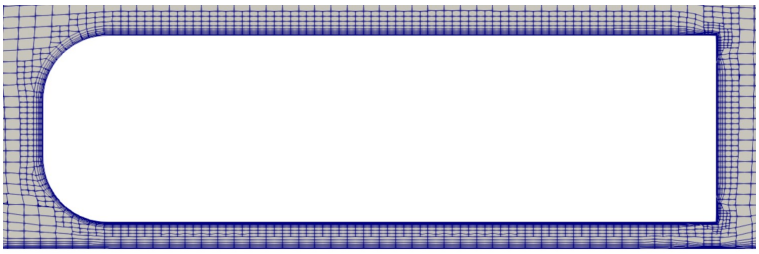

FIGURE 4.5: Close up of the mesh around the 0° diffuser configuration Ahmed body surface

In addition to observing the mesh around the geometry, the mesh created on the geometry should also be checked to avoid convergence problems. Selecting just the ahmed wall in ParaView, the mesh in Fig. 4.6 is shown. The critical parts are principally the edges and the curve zones at the front of the Ahmed body. This zones could present mesh errors if the meshing process wasn't done properly, thing that could lead to mistaken results. In Fig. 4.6 (a), the front mesh presents correct curve refinement zones as well as in Fig. 4.6 (b), the edges at the rear of the body are well defined and refined.

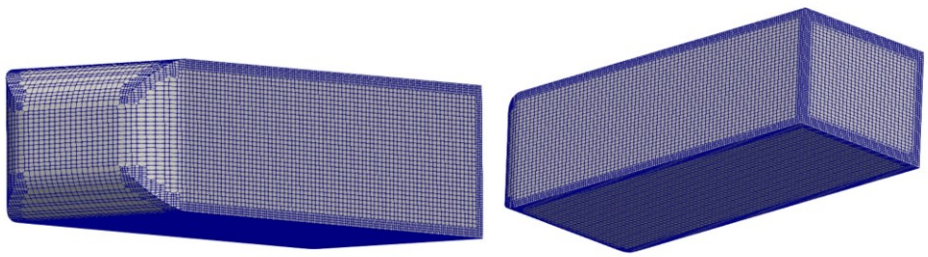

(a) (b)

FIGURE 4.6: Detailed 0° diffuser Ahmed body mesh at the (a) front and (b) rear parts of the geometry

The total number of cells in the mesh is 1,108,684. Once the mesh is done, the *checkMesh* command is run to verify that the quality of the mesh is good enough to proceed to the solver. This function provides the principal parameters that characterize the mesh The most important aspects to consider when checking the mesh quality are the following:

- Max aspect ratio. It defines when an element of the mesh presents its sides of different length. Hence, it measures the deviation of these sides from being being having the same length. A high aspect ratio occurs with long, thin elements for instance. High values does not affect significantly the stability of the solver, but could affect the convergence speed by decreasing it. The maximum aspect ratio obtained is 36.728, which is a high value but it can be considered inside an acceptable range due to the lack of computational resources.
- Skewness. Deviation between the shape of the cell and the shape of an equilateral cell of equivalent volume. Normally, in meshes with hexahedral cells, skewness should not exceed 0.85. Nevertheless, in the case of large 3D meshes larger values are acceptable. If skewness was reduced to less than unity, the mesh would have more than ten million cells. For this reason, the range of acceptable values of this parameter is set to 4-20. Higher values could affect the accuracy of the results and affect the stability of the solution. The maximum value of skewness obtained is 2.483, value below the minimum value which is considered acceptable for the case and taking into account the computational resources.
- Non-orthogonality. This parameter represents the angle between the line that connects the centres of two cells and the normal of their common face. The optimum value would be 0°, but a mesh of millions of cells would be needed. For this reason, a maximum is set to 75° with the use of nonOrthoCorrectors added in the fvSolutions file, precisely 3 of these correctors are applied on the pimpleFoam solver.

  The maximum non-orthogonality of the mesh is 72.508° with an average value of 6.148°. As the maximum value is below the value established as acceptable, the mesh is considered as good.

As mentioned before, these parameters show reasonable values taking into account the computational resources. They could be improved by adding more cells on each axis direction in the *blockMeshDict*, or increasing the level of refinement in the *snappyHexMeshDict*. However, being these parameters within the acceptable ranges for proper mesh quality, the mesh is given as good proceeding to obtaining results.

4.4.3 Post-process

With the mesh done, the simulation is performed. As stated in Sec. 4.1, first *potentialFoam* is run to initialize the steady-state solver. The steady-state solution converges after 329 iterations with a value of the lift coefficient of $C_L = -0.19$ and drag coefficient $C_D = 0.3$. Then the transient solver is initialized from the last time of the steady-state solution. At the same time the simulations calculate the pressure and velocity distributions, the force coefficients – lift and drag – are obtained for each iteration. The reference area to calculate these coefficients is the front area with a value of 0.029 m^2 (see Annex B.3.6). The velocity and pressure distributions observed with ParaView are presented below.

Velocity distribution

In Fig. 4.7 and 4.8, the velocity distribution around the Ahmed body is shown. The largest velocities are concentrated at the bottom of the body where the flow is directed towards the exit of the, in this case, the 0° diffuser. Due to there is no diffuser that smoothens the transition of the flow from underneath the body to the free-stream, it can be seen an abrupt change in velocity between the flow underneath the body and the velocity of the flow at the rear region of the body. Under the body, the flow shows a colour red meaning top velocity 27 m/s, while the wake that appears at the back of the body shows very small velocities, around 0-5 m/s. This phenomenon is what doesn't enable the negative lift to be as high as desired.

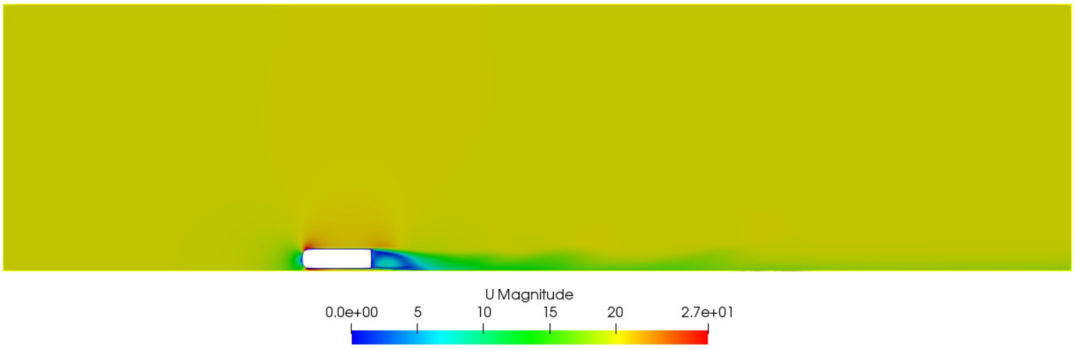

FIGURE 4.7: Velocity distribution around 0° diffuser0° diffuser Ahmed body

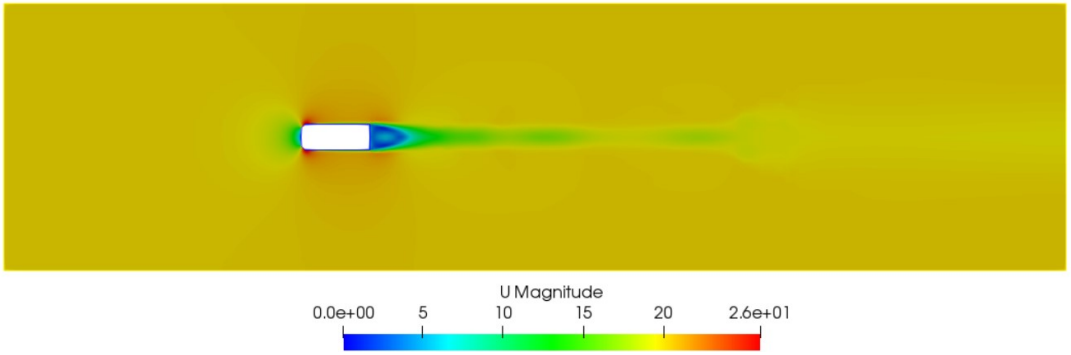

FIGURE 4.8: Velocity distribution top view around 0° diffuser0° diffuser Ahmed body

Furthermore, the other aspect to bear in mind is the generation of the vortex. With the help of the stream tracer tool in ParaView, the streamlines around the Ahmed body can be observed in Fig. 4.9. Two vortex generate at each side of the rear of the Ahmed body. However, they are concentrated at the rear bottom of this region, and they are not very large in size. As seen in the theoretical approach in Sec. 3.7, the bigger the vortex (up to a point) the better for the generation of lift. For this reason, in this case the downforce generated is quite small as the vortex are not developed well due to the abrupt transition of the flow from the underbody to the free stream. The vortex are somehow constraint by the end of the body as they do not have the space to be developed, since there is not a diffuser at the back of the body where they would generate at the diffuser inlet — see next case in Sec. 4.5.3. A comparison between the vortex generated on the three cases of study will be done in order to understand better the function of these.

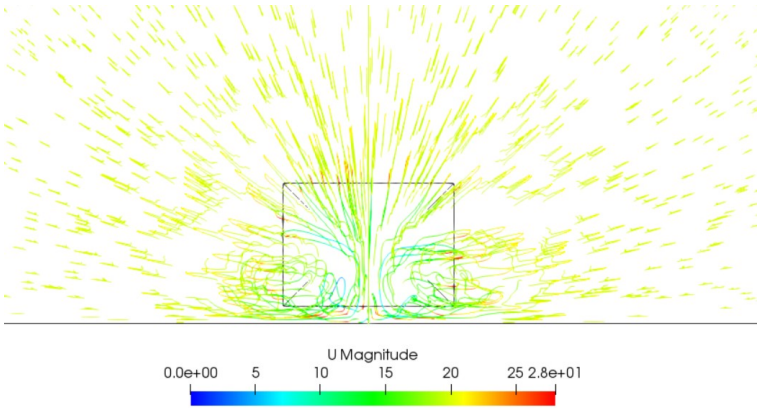

FIGURE 4.9: Streamlines on the rear part of 0° diffuser Ahmed body

Pressure distribution

The pressure distribution around the Ahmed body is shown in Fig. 4.10. A zone of low pressure or suction appears underneath the Ahmed body due to the large velocities in this region seen previously.

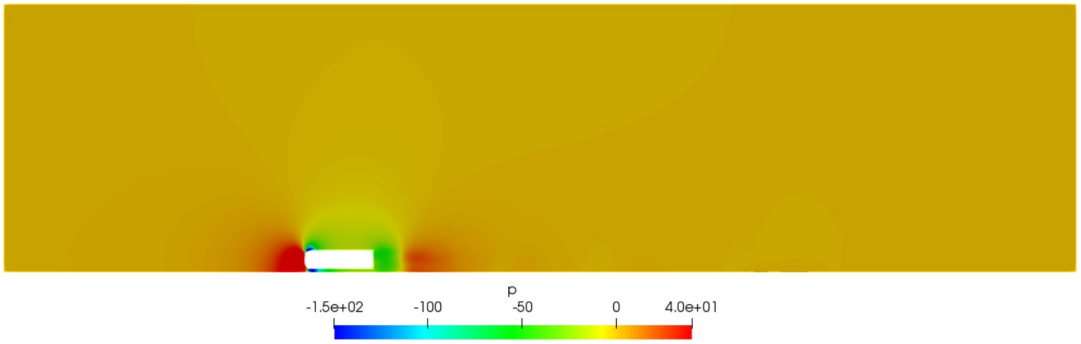

FIGURE 4.10: Pressure distribution around 0° diffuser Ahmed body

4.4.4 Results

The steady-state solution converged after 329 iterations until resulting in the following values of lift and drag coefficients:

$$C_{L_{ahmed\ 0^\circ}} = -0.179 \qquad C_{D_{ahmed\ 0^\circ}} = 0.306$$

The minimum slant angle simulated in Fig. 3.8 of 5° shows a value of $C_L = -0.6$. Otherwise, in Fig. 3.6 the 0° diffuser configuration is simulated obtaining a $C_L = -0.16$ approximately. From these values, the value obtained of the lift coefficient is considered reasonable as it is very similar to the one of Fig. 3.6 [8]. Furthermore, from the results of [14] observing the difference in lift coefficient between the 5° and 10° diffusers, 0.6 and 0.8 approximately, it is clear that if the 0° diffuser configuration was simulated the value of lift coefficient will decay to a value close to the one obtained in this study. However, these articles are taken as reference to validate that the results obtained are reasonable. If the results differed very much, they could not be taken as acceptable – the simulation should be redone.

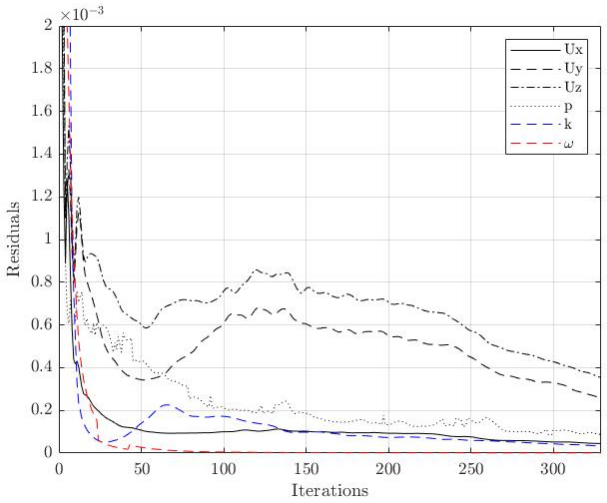

FIGURE 4.11: Representation of the steady-state solution residuals of 0° diffuser Ahmed body

In Fig. 4.11 the residuals in the steady-state solution of the velocities U_x, U_y and U_z, pressure p, turbulent kinetic energy k and the specific turbulent dissipation rate ω are presented. The residuals decay for each iteration. The final residuals of U_x, the pressure, k and ω are very small. The residuals of velocities U_y and U_z are slightly bigger than the previous mentioned, but still are very small. All these residuals decrease up to a point, where each plot reaches its minimum value, in other words, where the solution converges. When reaching these very small values, the solver stops as the residuals are small enough to provide a good solution.

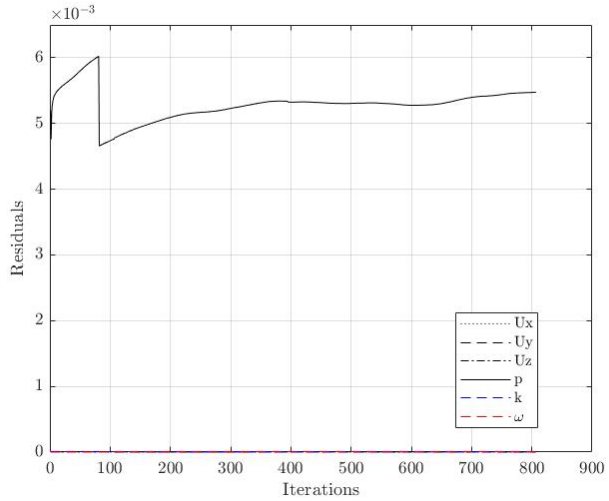

FIGURE 4.12: Representation of the transient solution residuals of 0° diffuser Ahmed body

After obtaining a converged solution of the steady solver, the transient solver is initialized. The Δt was of the order of magnitude of 10^{-5}, set by OpenFOAM© adjusting it considering a maximum Courant number of 1.5. Starting from the pressure and velocity fields from the steady solution, the transient solver is initialized and finalizes after 806 iterations. The final residuals of these solutions are shown in Fig. 4.12. All the residuals are practically 0, except the final residual of the pressure that

increases substantially to a value of $6 \cdot 10^{-3}$. Even though being this value still small, its abrupt increase is something to highlight.

Despite of the strange behaviour of the pressure residual, the transient solution of the lift and drag coefficients stabilize to approximately -0.18 and 0.28, respectively as shown in Fig. 4.13 and 4.14. It can be seen that the results remain practically constant for the last 600-700 iterations. This stable solution can be given as acceptable, hence the mesh is considered as a good quality mesh thanks to the stable results it provides.

$$C_{L_{ahmed\ 0^\circ}} = -0.182 \qquad C_{D_{ahmed\ 0^\circ}} = 0.287$$

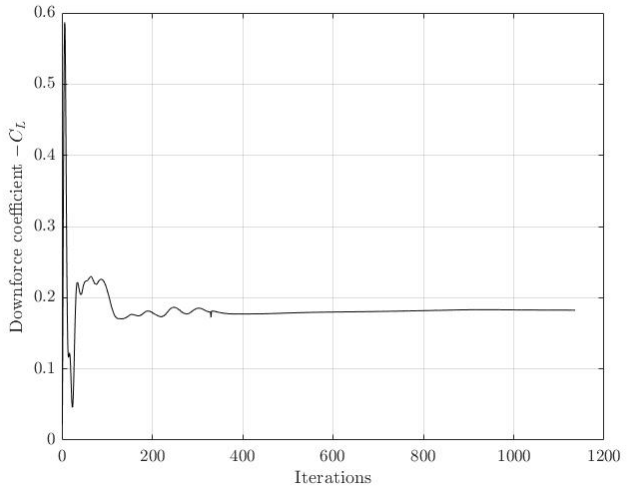

FIGURE 4.13: Representation of the downforce coefficient $-C_L$ of 0° diffuser Ahmed body

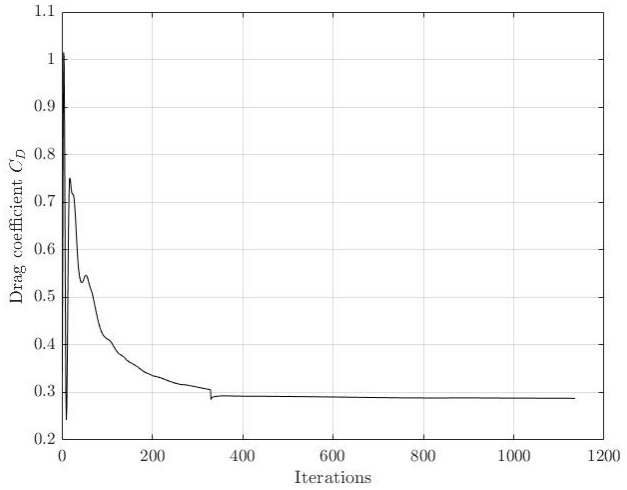

FIGURE 4.14: Representation of the drag coefficient C_D of 0° diffuser Ahmed body

These results make sense as it is a simple Ahmed body configuration in which the

only factor that generates lift is the ground effect, even though not as much as desired. The downforce coefficient is rather small, as well as the drag. This was predictable due to the non-diffuser configuration. To observe how the presence of a diffuser affects the downforce generation under the same simulation conditions, in the following section a 25° diffuser is added to the Ahmed body.

4.5 Ahmed body with $\theta = 25°$ diffuser

In this section, it is presented a simulation of the Ahmed body with a diffuser of 35% length and slant angle of 25° at a ride height of 20 mm. Observing Fig. 3.8 it is extracted that the diffuser configuration that gives the best performance is with a slant angle of 25° at a ride height of 20 mm, with a lift coefficient of $C_L = -1.4$ and an aerodynamic efficiency $-C_L/C_D = 3$, corresponding to a drag coefficient of $C_D = 0.470$ approximately. This diffuser configuration is selected so as to observe the flow behaviour of an optimal diffuser configuration.

4.5.1 Geometry

The Ahmed body configuration used in this case is described in Sec 3.2, where its dimensions are exposed. As mentioned for the previous case (see Sec. 4.4.1) the standardized model of the Ahmed body is not used in this study, but the model shown in Fig. 4.15 with the corresponding dimensions from [14]. In contrast with the previous case, this Ahmed body geometry incorporates a diffuser with slant angle of 25° in its bottom rear part, with a diffuser length of 182 mm (35% of the total body length).

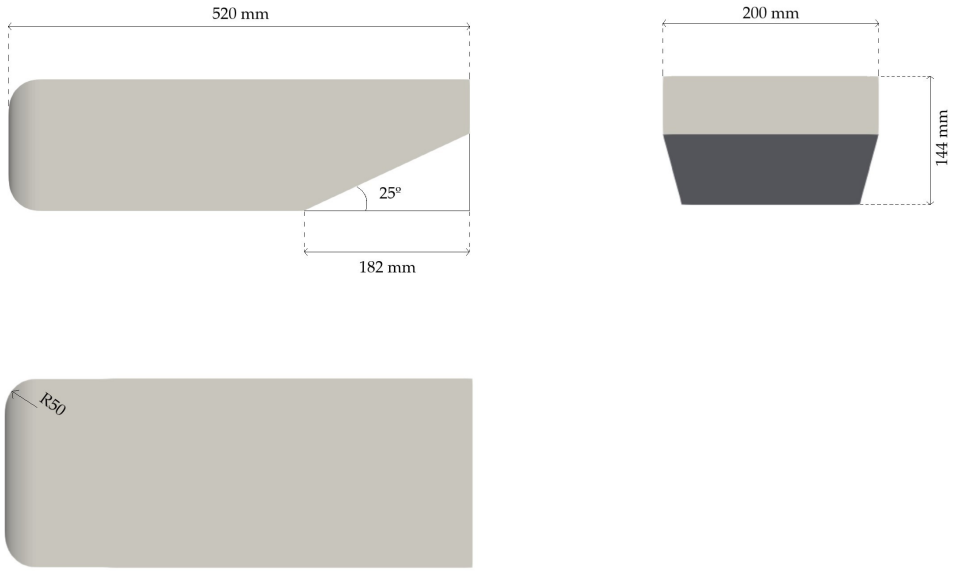

FIGURE 4.15: Dimensions of the 25° diffuser Ahmed body geometry used

4.5.2 Meshing

The meshing process followed for this Ahmed body configuration is the same as described for the previous case in Sec. 4.4.2. The mesh obtained has 1,456,999 cells. The

side and top views of the mesh are presented in Fig. 4.16 and 4.17. The mesh conditions are similar to the ones in the previous case, but some parameters are changed – see Annex B.3.4. The features and surface level of refinement are increased to 7 and (6 6), respectively. Additionally, the level of refinement of the ground and wake refinement regions are increased to (4 4). These rises are done with the aim of better meshing the regions where more cells are necessary, as can be the edge of the diffuser inlet or the region between this diffuser and the ground. The rear part mesh of the geometry must be checked carefully to avoid any mesh complication. On the top view of Fig. 4.17, it is clearly seen how refinement regions created surround the body concentrating the cells around it. The smaller refinement region, called refinement wake, concentrates the major part of the cells around the geometry, giving special treatment to those critical zones of the Ahmed body.

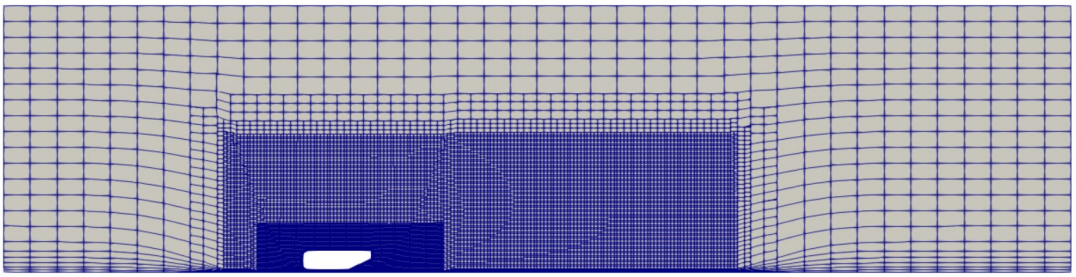

FIGURE 4.16: Side view of the mesh of the Ahmed body with 25° diffuser configuration

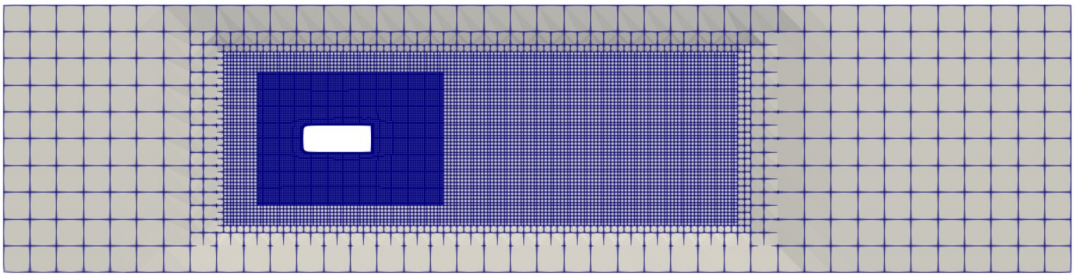

FIGURE 4.17: Top view of the mesh of the Ahmed body with 25° diffuser configuration

In this case, the edge delimiting the diffuser intlet must be given special treatment since its sharp angle if not refined enough could give convergence problems. Balancing between computational capability and mesh quality, the level of refinement around the Ahmed body surface was set to (2 3) as in the previous case. This level seemed to give a good refinement in the zones required (see Fig. 4.18).

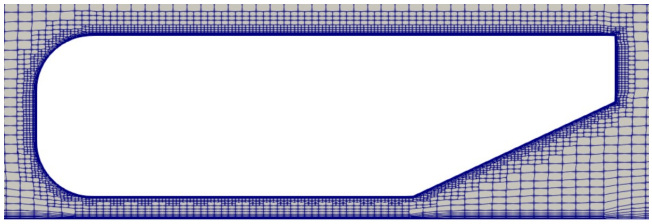

FIGURE 4.18: Close up of the mesh around the 25° diffuser configuration Ahmed body surface

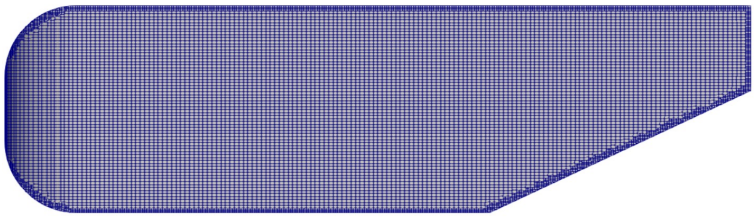

FIGURE 4.19: Detailed 25° diffuser Ahmed body side view mesh

In Fig. 4.19, the side view of the surface mesh of the geometry can be observed. An structured mesh is created with a higher level of refinement on the edges as these are critical for the solver. Regarding the curved zones at the front, they present a good refinement as observed in Fig. 4.20 (a). Moreover, for the edges contained in the diffuser no complication was observed and the refinement was good – see Fig. 4.20 (b). The surface refinement compared to previous case in Fig. 4.6 is clearly more refined over the whole surface.

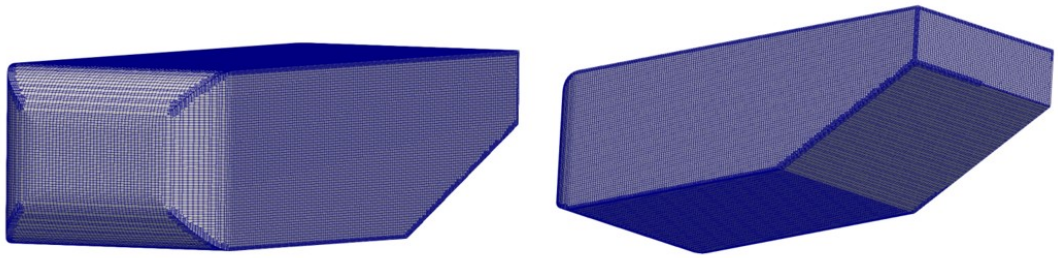

FIGURE 4.20: Detailed 25° diffuser Ahmed body mesh at the (a) front and (b) rear parts of the geometry

Running the *checkMesh* command, the maximum aspect ratio obtained is 37.859, slightly smaller value than in the 0° diffuser configuration, which is considered acceptable. The maximum value of skewness obtained is 2.683, below the minimum, hence it is considered acceptable. Finally, the maximum non-orthogonality of the mesh is 73.699° with an average value of 6.719°. The maximum value is slightly below the value established as acceptable, but the mesh can be considered as good.

4.5.3 Post-process

As for the previous case, once the desired mesh is obtained the simulation can begin. The steady-state solution converges after 221 iterations with a value of the lift coefficient of $C_L = -1.525$ and drag coefficient $C_D = 0.545$. From the last time of the steady-state solution, the transient solver is initialized. The velocity and pressure distributions for the steady-state and the transient solutions observed with ParaView are presented below.

Velocity distribution

In Fig. 4.21, 4.22 and 4.23, the velocity distribution around the Ahmed body for the steady-state and the transient solutions is shown. In this case, the largest velocities are clearly more concentrated at the underbody where the flow is directed towards the diffuser outlet. With the presence of the 25° diffuser, the transition of the flow from larger velocities of around 20-26 m/s to the free-stream is clearly smoother than

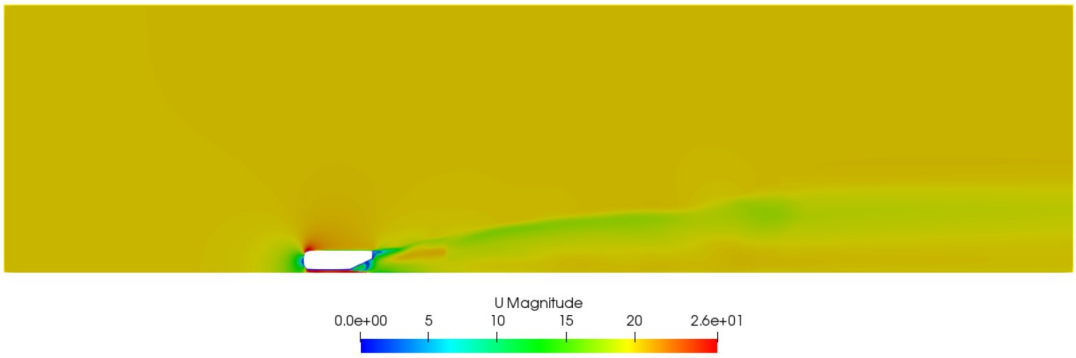

FIGURE 4.21: Velocity distribution of the steady-state solution on the 25° diffuser configuration

in the case of the non-diffuser Ahmed body. The steady-state and transient velocity distribution are very similar, but the **transient shows a smoother transition of the flow velocity leaving from the diffuser inlet to the outlet**. This higher velocity at the underbody, as for the Venturi effect, will imply a reduction in the pressure on this region, which enhances the generation of lift on the body. The wake produced at the back of the body is more significant than the one observed in Fig. 4.7 for the previous case. This is also due to the smoother transition of the flow thanks to the presence of the diffuser.

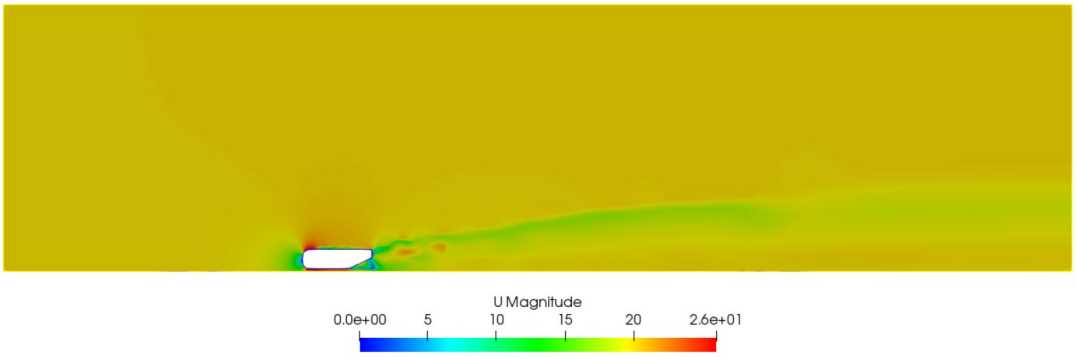

FIGURE 4.22: Velocity distribution of the transient solution on the 25° diffuser configuration

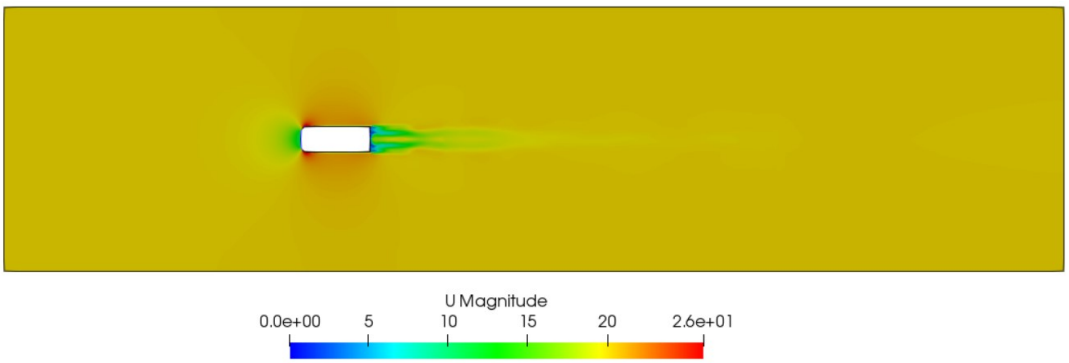

FIGURE 4.23: Velocity distribution top view of the transient solution on the 25° diffuser configuration

Observing the streamlines of the flow leaving the diffuser in Fig. 4.24, the vortex generated at the diffuser inlet are shown. As can be observed in the figure, these

vortex are the responsible of the wake generated. They spin until reaching the free-stream where the wake is smoother and eventually, finishes as the free-stream flow.

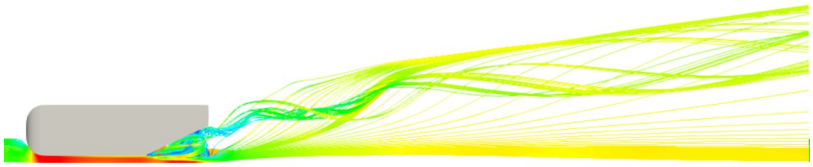

FIGURE 4.24: Streamlines representing the velocity field in the wake leaving the diffuser's outlet

For a better visualization of the vortex and their size, a rear view of the streamlines of the body is presented in Fig. 4.25. The size of the vortex are clearly larger than in the case of the 0° diffuser, approximately 3 or 4 times larger than the Ahmed body dimensions. Two vortex are observed, one at each side of the diffuser. The left vortex rotates at the counterclockwise direction, while the right one rotates at the opposite direction, in the clockwise direction. This verifies the phenomenon predicted by the vortices theoretical approach in Sec. 3.7. Furthermore, as was also stated in that section, as bigger the vortex, larger the lift generation, thing that is accomplished as the lift coefficient obtained is much bigger than the one obtained for the non-diffuser configuration.

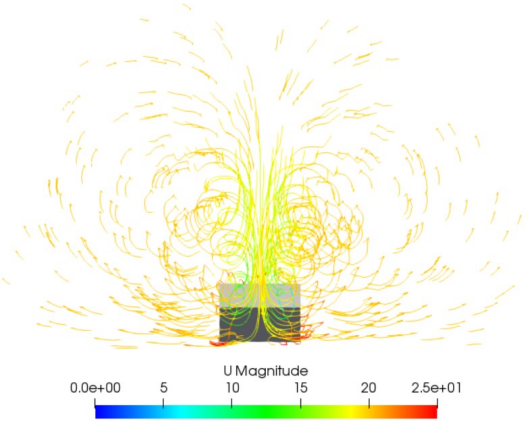

FIGURE 4.25: Streamlines of the velocity field at the back of the 25° diffuser configuration Ahmed body

Pressure distribution

The pressure distribution around the Ahmed body is shown in Fig. 4.26. Just the pressure distribution of the transient solution is shown as the steady-state was very similar. This images ratify the statements mentioned before: as there are larger velocities underneath the body, the suction zone in this region is clearly more accentuated, which ratifies the use and addition of a diffuser in vehicles as the suction is larger, the adhesion on the track will be better improving the cornering the speed.

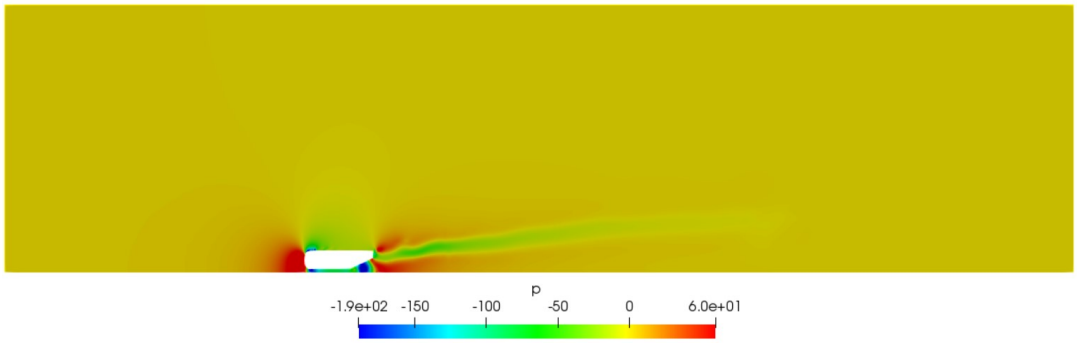

FIGURE 4.26: Pressure distribution of the transient solution on the 25° diffuser configuration

4.5.4 Results

On the first place, the steady-state solution for the 25° diffuser Ahmed body converged after 211 iterations obtaining the following values of lift and drag coefficients:

$$C_{L_{ahmed\ 25°}} = -1.525 \qquad C_{D_{ahmed\ 25°}} = 0.545$$

In Fig. 4.27 the residuals of this steady-state solution are presented. The residuals decay for each iteration. Similar to the previous case, the final residuals of U_x, the pressure, k and ω are very small, but the ones for velocities U_y and U_z are slightly bigger than the previous mentioned, but still small. In the point where each plot reaches its minimum value is where the solution converges.

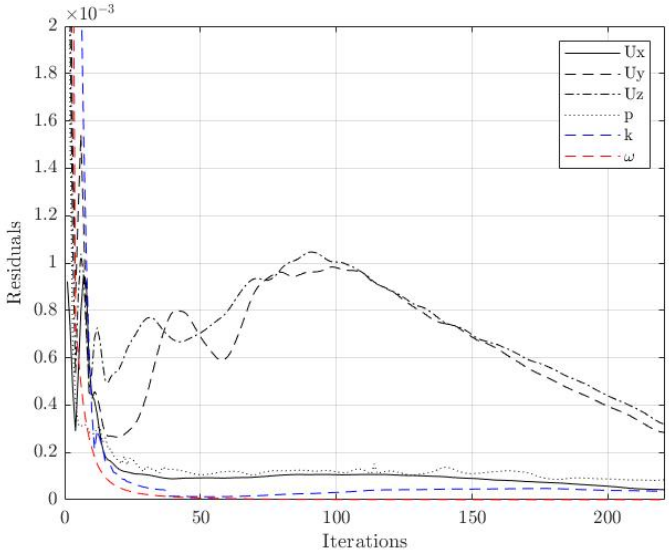

FIGURE 4.27: Representation of the steady-state solution residuals of 25° diffuser Ahmed body

In Fig. 3.8 for the 25° at a ride height of 20 mm, the value of the lift coefficient is between -1.4 and -1.45 and the aerodynamic efficiency $-C_L/C_D$ is approximately 3, implying a drag coefficient C_D of 0.47 - 0.48. The values are very close and they

can be considered acceptable as the error is of the 4%. With the application of the transient solver, this values can change reaching closer values.

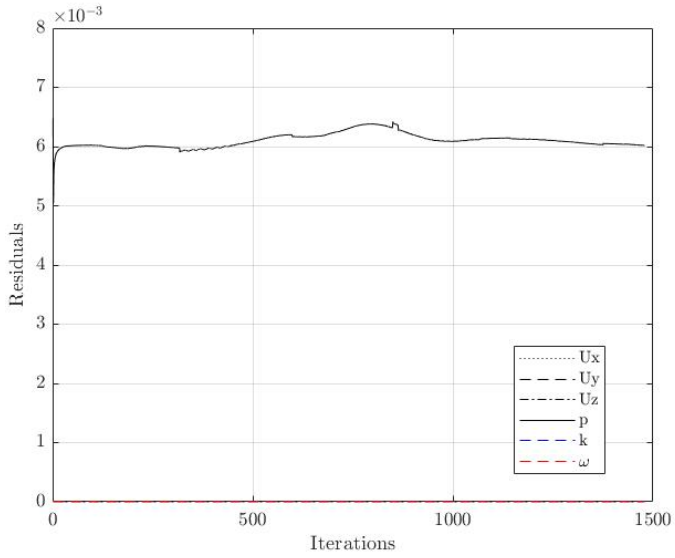

FIGURE 4.28: Representation of the transient solution residuals of 25° diffuser Ahmed body

Running the *pimpleFoam* transient solver, new values of the lift and drag coefficients are obtained. The total number of iterations are 1479. Fig. 4.28 show the residuals of the transient solution, in which all the parameter's residuals show very small values close to 0. However, the pressure residual is increased to $6 \cdot 10^{-3}$, large with respect to the other parameters but still small to consider these residuals acceptable.

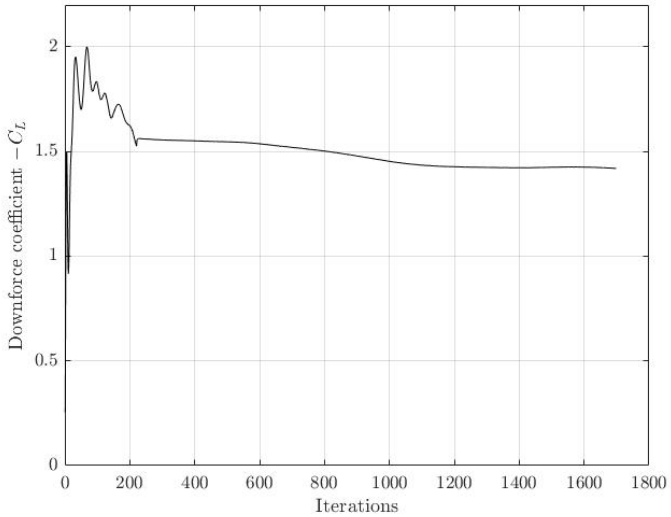

FIGURE 4.29: Representation of the downforce coefficient $-C_L$ of 25° diffuser Ahmed body

Observing the plots of the lift and drag coefficient for each iteration in Fig. 4.29 and 4.30, it is shown that from iteration number 1200, the values for both coefficients stabilize. It can be taken as acceptable that the last 400 iterations, for the 27% of the

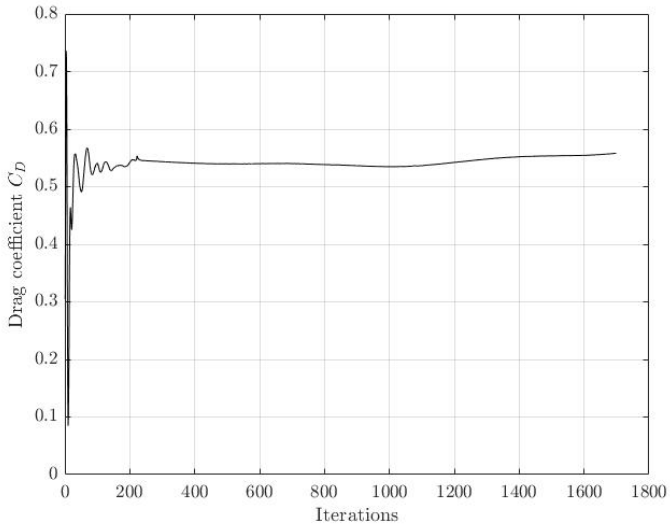

FIGURE 4.30: Representation of the drag coefficient C_D of 25° diffuser Ahmed body

simulation, the values remain practically constant. The definitive values of these coefficients are:

$$C_{L_{ahmed\ 25^\circ}} = -1.419 \qquad C_{D_{ahmed\ 25^\circ}} = 0.558$$

This lift coefficient is closer to the value of lift coefficient $C_{L_{ahmed\ 25^\circ}} = -1.45$ approximately, obtained in Fig. 3.8 [14]. However, the drag coefficient still is further from the reference value of $C_{D_{ahmed\ 25^\circ}} = 0.48$. This could be due to the mesh, as the solver can find some trouble with some cells and more drag can be considered that is generated. Otherwise, downforce has substantially increased compared to the non-diffuser case, as well as the drag.

Finally, in the next section two airfoils are added one at each side of the diffuser outlet. This case is proposed by former Ferrari aerodynamics engineer, Willem Toet, in order to generate a low pressure zone at the back of the geometry and increase the downforce generated.

4.6 Ahmed body with rear airfoils configuration

The last simulation is presented in this section. The geometry consists of an Ahmed body with a diffuser of 35% length and slant angle of 25° at a ride height of 20 mm – as in Sec. 4.5 – but two airfoils are added at each side of the rear part of the diffuser. It is the most complex simulation done by far in this study due to its complex geometry containing some accentuated sharp angles. The simulation of this geometry was proposed by Willem Toet, former Scuderia Ferrari aerodynamicist. The aim of the addition of the airfoils was to create a zone of low pressure (suction) at the back of the trailing edge of the body. For this reason, there is no reference of results for this geometry. Nevertheless, principally it should be observed an increase in the downforce coefficient.

4.6.1 Geometry

The geometry was created with Solidworks© starting from the 25° diffuser Ahmed body and following the scheme presented in Fig. 4.31. Two airfoils were drawn and then extruded with the same height of 144 mm as the Ahmed body.

FIGURE 4.31: Two-dimensional scheme of the geometry provided by Willem Toet

Fig. 4.32 presents the final geometry obtained. The Ahmed body is the same as in Sec. 4.5 wih the addition of two airfoils at each side of the diffuser exit – the airfoils were drawn from scratch, they do not represent any type of NACA airfoil. The closest point of the airfoil is located at a distance 50 mm of from rear of the Ahmed body.

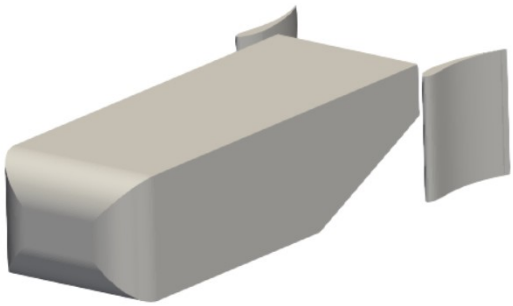

FIGURE 4.32: Geometry of the 25° diffuser Ahmed body with airfoils added at the rear

4.6.2 Meshing

The mesh for this case is similar as in the case with no airfoils. However, a refinement region surrounding the region of the airfoils is added in the *snappyHexMeshDict* – see Annex B.3.5– to better capture the sharp angles at the trailing edge of the airfoils (see Fig. 4.35). The level of features refinement is increased to 7 to better refine these sharp regions of the geometry. Furthermore, the level of refinement of the surface is also increased to (6 7).

With these modifications with respect to the previous case, the mesh created has 1,552,709 cells, way more than in the previous two cases due to the high refinement around the airfoils. Despite of the increase in refinement done, this geometry is significantly difficult to mesh due to the sharpness of the rear airfoils.

The side views of the mesh in Fig. 4.33 and 4.34 are very similar to the meshes of the previous two cases. However, the refinement region surrounding the Ahmed body is more concentrated closer to the geometry and with higher level of its refinement. From the top view it is clear the difference in the mesh as the cells can be seen in Fig.

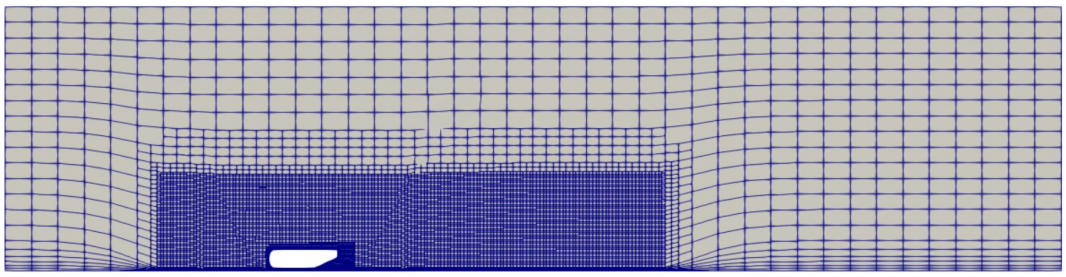

FIGURE 4.33: Side view of the mesh of the Ahmed body with rear airfoils 25° diffuser configuration

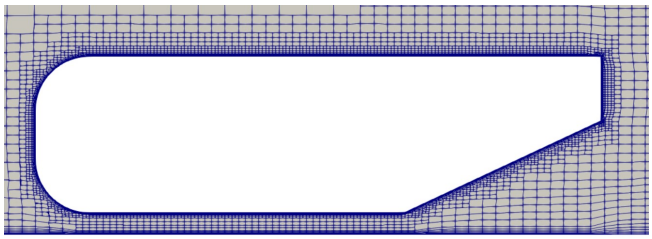

FIGURE 4.34: Close up mesh around the rear airfoils Ahmed body

4.35 more concentrated closer to the airfoils region. Despite of this concentration of cells around the geometry surface, a better refinement should be done but due to the actual computational resources no further refinement could be done.

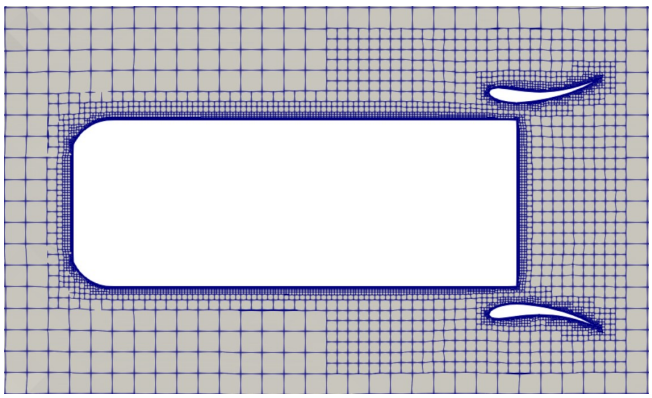

FIGURE 4.35: Close up of the top view mesh around the rear airfoils 25° diffuser configuration Ahmed body surface

Regarding the surface refinement of the Ahmed body geometry, it can be clearly observed that in Fig. 4.36 there are more cells and they are more concentrated compared to the previous case in Fig. 4.20. Fig. 4.36 (a) shows a good refinement of the front area of the Ahmed body. And in Fig. 4.36 (b) the mesh at the rear of the Ahmed body as well as in the airfoils is presented, showing greater refinement at the trailing edge of these airfoils. Cells are clearly more concentrated at the trailing edge, comparing it to the rest of the geometry.

A close-up of the critical edges is shown in Fig. 4.37. Fig. 4.37 (a) shows a detailed top view of the airfoils, which have great level of refinement without presenting any meshing error in the sharp angles. Additionally, Fig. 4.37 (b) shows a side view of one airfoil. The level of refinement decreases from the left to the right – from trailing

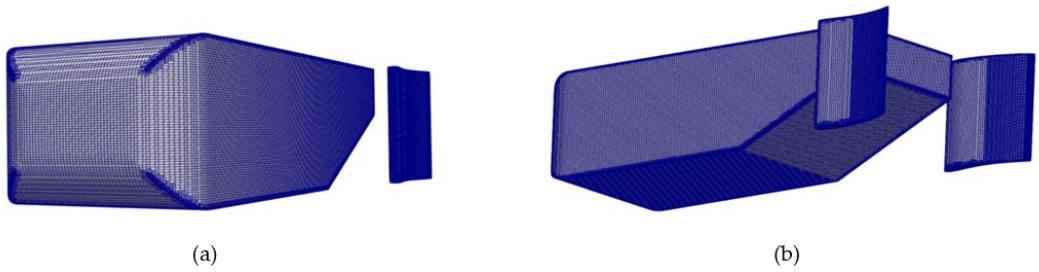

(a) (b)

FIGURE 4.36: Detailed rear airfoils 25° diffuser Ahmed body surface mesh at the (a) front and (b) rear parts of the geometry

edge to leading edge. Cells must be more concentrated in the trailing edge due to the extremely shallow angle on this region. Moreover, as the leading edge has a curve geometry but not as critical as the trailing edge, the concentration of cells is not significantly needed. However, the level of refinement is enough considering the type of curvature.

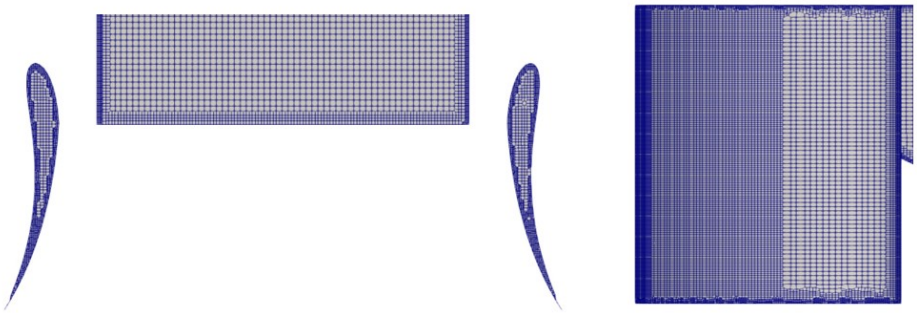

(a) (b)

FIGURE 4.37: Detailed surface mesh of (a) top view and (b) side view of the rear airfoils

Finally, from the *checkMesh* function it is obtained that the maximum aspect ratio obtained is 37.740, which is a high value but, as in previous cases, it can be considered inside an acceptable range. The maximum value of skewness obtained is 5.741, value slightly higher than the minimum value of 4. However, due to the large number of cells already and the computational resources, this value is considered acceptable as it is within the range of skewness established. The maximum non-orthogonality of the mesh is 73.644° with an average value of 9.424°. As the maximum value is below the value established as acceptable, the mes is considered as good.

4.6.3 Post-process

Finally, the last simulation is run first with the *simpleFoam* and then with the *pimpleFoam*. The steady-state solution converges after 405 iterations resulting in a lift coefficient of $C_{L_{rear\ airfoils}} = -2.059$ and a drag coefficient of $C_{D_{rear\ airfoils}} = 1.053$. Then from the last time of the steady-state solution, the transient solver is initialized. The velocity and pressure distributions for the steady-state and the transient solutions observed with ParaView are presented below.

Velocity distribution

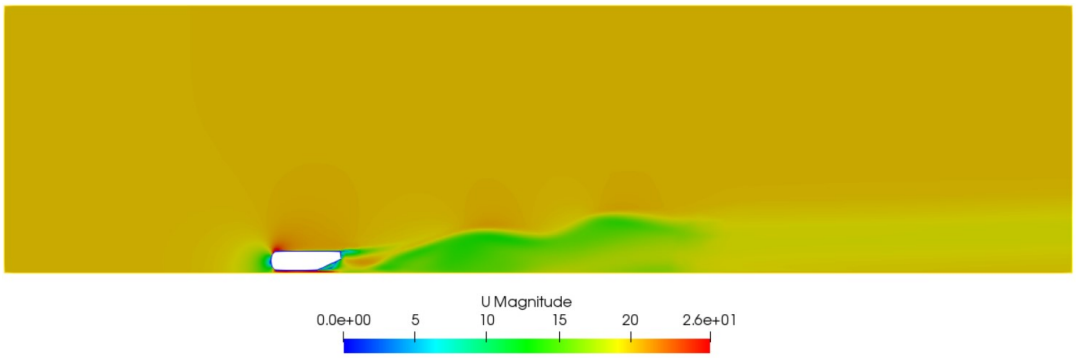

FIGURE 4.38: Velocity distribution of the steady-state solution of the rear airfoils 25° diffuser configuration

The velocity distribution around the rear airfoils 25° diffuser Ahmed body for the steady-state and the transient solutions appear in Fig. 4.38 and 4.39. As observed in the previous case, the largest velocities are concentrated at the underbody where the flow is directed towards the diffuser outlet. A clear difference between the steady-state and transient velocity distributions can be observed in the wake generated on both, where in the transient shows a more distorted transition of the flow velocity leaving diffuser. This is due to the more accentuated vortex generated by the rear airfoils. Compared to the case with no airfoils in Fig. 4.22, the wake is also less smooth for the case with airfoils.

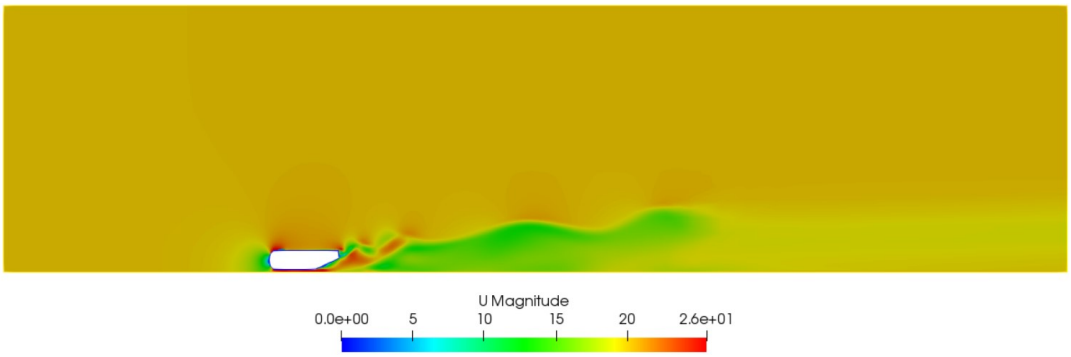

FIGURE 4.39: Velocity distribution of the transient solution of the rear airfoils 25° diffuser configuration

Observing the velocity distribution from the top of the geometry, it is observed how the rear airfoils affect the shape and behaviour of the wake. The airfoils lead the flow leaving the diffuser creating a low pressure zone – as there's a region inside where the is larger – in this rear region just after the diffuser outlet. This low pressure zone helps smoothing the transition from the underbody to the free-stream of the flow.

Using the stream tracer function of ParaView, the streamlines of the flow leaving the diffuser can be observed in Fig. 4.41. The vortex generated at the diffuser inlet are shown. As can be observed in the figure, these vortex seem more organized than in the case of the 25° diffuser configuration. In this case, the wake is smaller, which in a race when following a car to overtake, smaller wakes are proven to be better as less "dirt" air is thrown to the car behind and overtaking gets easier.

In Fig. 4.42, the view of the streamlines on the underbody can also be observed. It can be observed how the 2 vortex generate at the diffuser inlet and how they develop

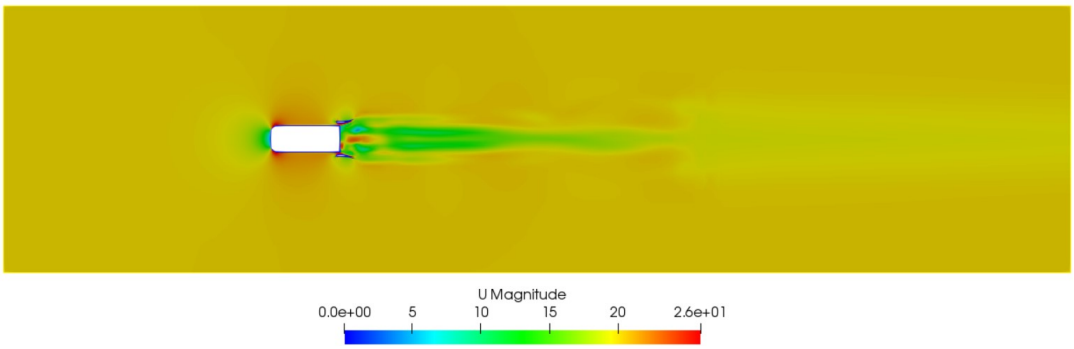

FIGURE 4.40: Velocity distribution top view of the transient solution of the rear airfoils 25° diffuser configuration

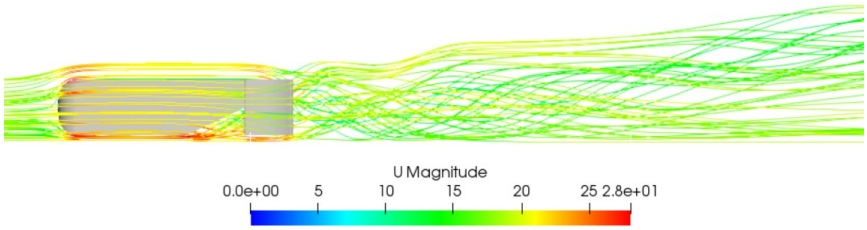

FIGURE 4.41: Streamlines of the wake leaving the diffuser's outlet

as they leave the diffuser outlet. In Fig. 4.43, it can be seen how these vortex leave this diffuser.

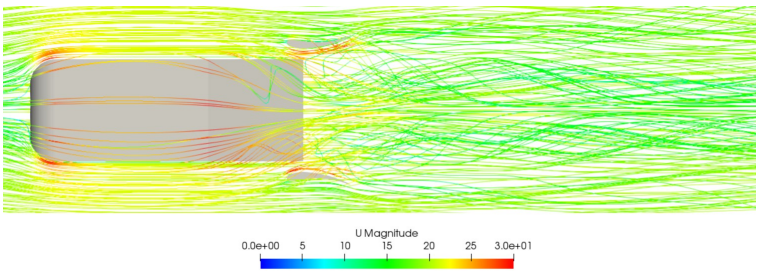

FIGURE 4.42: Streamlines of the velocity field at the underbody of the rear airfoils 25° diffuser configuration Ahmed body

The rear view of the streamlines of the flow around the body showing the vortex and their size is presented in Fig. 4.43. As in previous case, two vortex are observed, one at each side of the diffuser. The left vortex rotates at the counterclockwise direction, while the right one rotates at the opposite direction, in the clockwise direction. This verifies the phenomenon predicted by the vortices theoretical approach in Sec. 3.7. However, it seems that, besides the two main vortex, another 2 vortex appear at the bottom of the Fig. 4.43, each one going on the opposite direction than its main vortex above of them. This could be caused by the rear airfoils that guide the flow following the shape of the airfoils and could make the flow on the main vortex to change its direction.

Pressure distribution

The pressure distribution around the rear airfoils 25° diffuser configuration Ahmed body is shown in Fig. 4.44 and and 4.45. This images ratify the statements mentioned

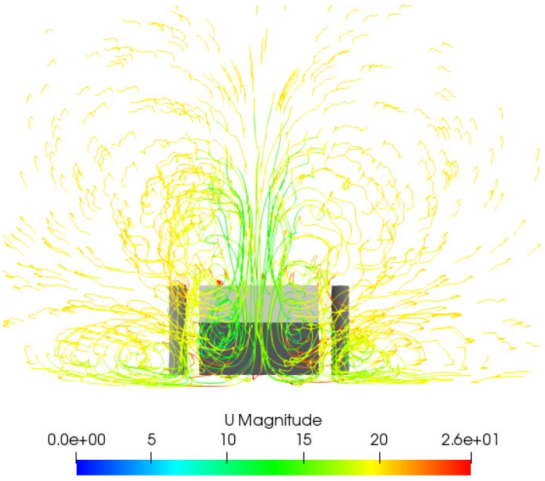

FIGURE 4.43: Streamlines of the velocity field at the back of the rear airfoils 25° diffuser configuration Ahmed body

before: as there are larger velocities underneath the body, the suction zone in this region is clearly more accentuated, which verifies the use and addition of a diffuser in vehicles as the suction is larger, the adhesion on the track will be better improving the cornering the speed. Compared to the previous case with no airfoils, in Fig. 4.45, it is clearly seen how the region below the diffuser and when leaving the diffuser, the pressure is lower than in Fig. 4.26 for the 25° diffuser. This confirms that the addition of two rear airfoils at the back of the Ahmed body creates a suction zone that improves the performance of the geometry as the lift coefficient is increased – see Sec. 4.6.4.

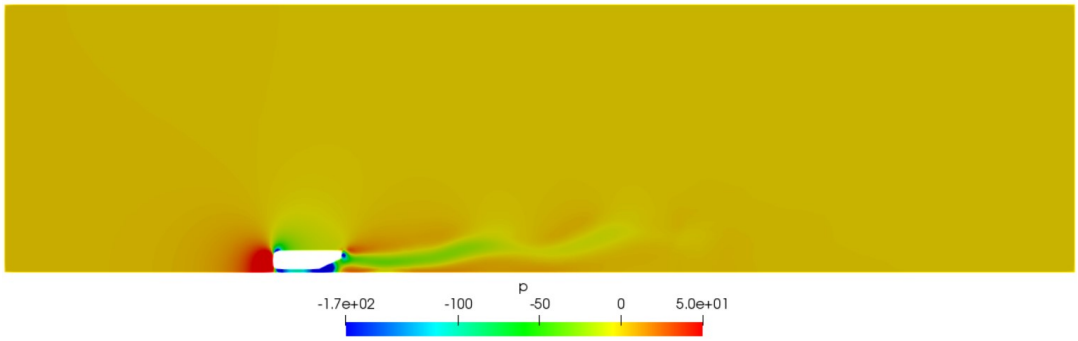

FIGURE 4.44: Pressure distribution of the steady-state solution of the rear airfoils 25° diffuser configuration

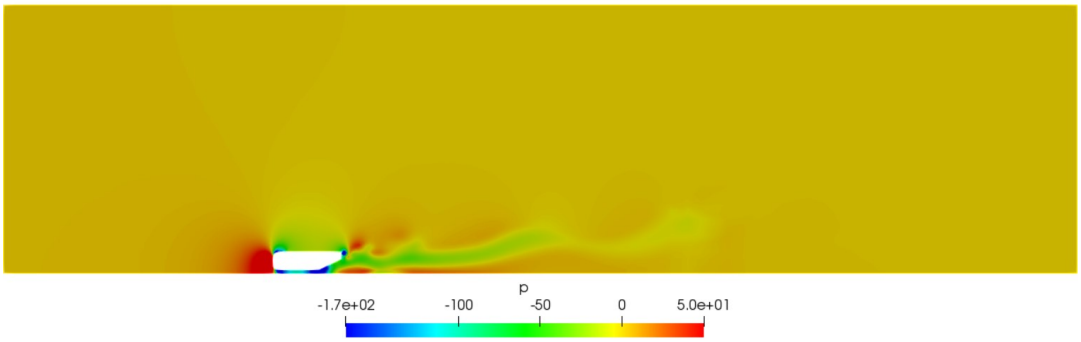

FIGURE 4.45: Pressure distribution of the transient solution the rear airfoils 25° diffuser configuration

4.6.4 Results

The steady-state solution for the rear airfoils 25° diffuser Ahmed body converged after 405 iterations obtaining the following values of lift and drag coefficients:

$$C_{L_{rear\ airfoils}} = -2.059 \qquad C_{D_{rear\ airfoils}} = 1.053$$

As there is no previous study of this geometry, no comparison between reference values and these can be done. However, the order of magnitude is correct, and the predicted lift was that it should increase with regard the previous two simulations done. For this reason, it is considered that these values obtained are acceptable. In the following Fig. 4.46 the residuals of this steady-state solution are presented. The residuals decay for each iteration. Similar to the previous case, the final residuals of U_x, U_y, the pressure, k and ω are very small, but in this case just the residuals of the velocity U_z are bigger than the previous variables, but they are still small values. At the final iteration 405, each plot reaches its minimum value and it is where the solution converges.

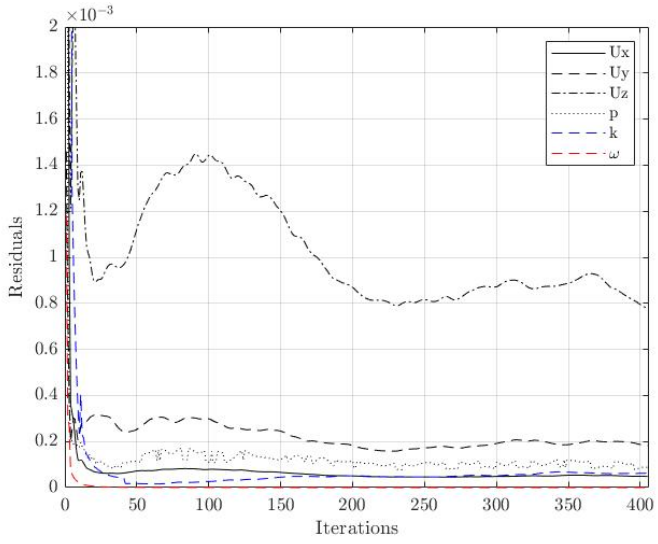

FIGURE 4.46: Representation of the steady-state solution residuals of rear airfoils Ahmed body

After running the transient solver, the results for the lift and drag coefficients change. The total number of iterations are 6500. In Fig. 4.47 the residuals of the transient solution are shown. All the parameter's residuals show very small values close to 0, except for the pressure residual which is increased to over $7 \cdot 10^{-3}$, large with respect to the other parameters but still small to consider these residuals acceptable.

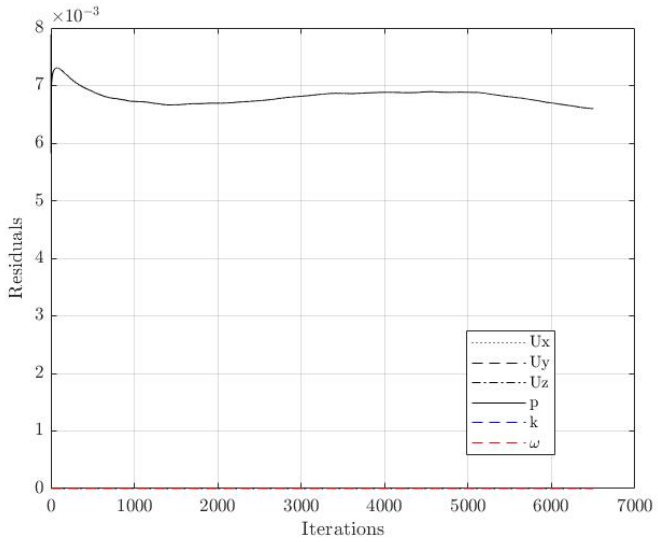

FIGURE 4.47: Representation of the transient solution residuals of rear airfoils Ahmed body

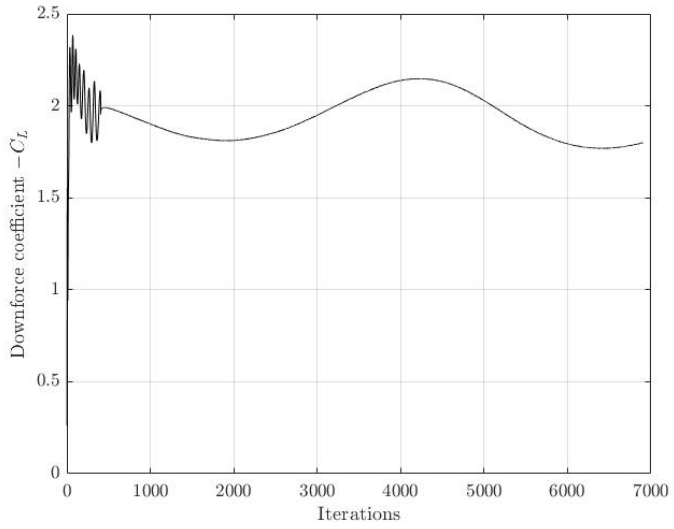

FIGURE 4.48: Representation of the downforce coefficient $-C_L$ rear airfoils Ahmed body

Lift and drag coefficient solutions fluctuate between a range of values: lift between -2.15 and -1.77 and drag between 1.07 and 1.05. This may indicate that there may be a problem of convergence with the mesh and a process of refinement of critical areas should be done in order to improve convergence. To take a reasonable solution, it has been chosen the approximate value of the lift coefficient as the solution that was constant over the major number of iterations during the whole simulation. The value

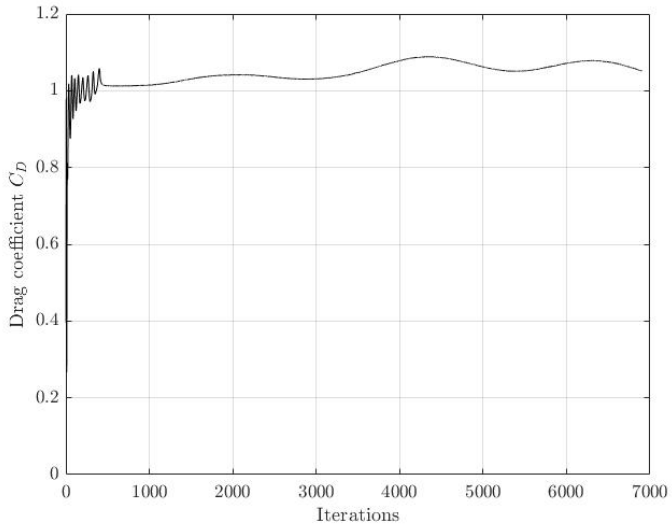

FIGURE 4.49: Representation of the drag coefficient C_D of rear airfoils Ahmed body

that was more repeated was $C_L = -2.14$ with $C_D = 1.08$, which remained constant over more than 400 iterations, 6% of the simulation.

$$C_{L_{rear\ airfoils}} = -2.14 \qquad C_{D_{rear\ airfoils}} = 1.08$$

This non-stable solution could be due to the mesh, as more cells may be needed to obtain more accurate results and improve convergence. However, considering the actual computational resources this results are considered as acceptable and reasonable. In the following Sec. 4.7, all the results obtained are compared and discussed.

4.7 Analysis of results

The simulation of the non-diffuser configuration in Fig. 4.50 (a) intends to act as a base geometry to compare to for posterior simulations. With no diffuser, the body itself produces downforce due to the ground effect when it is located close to the floor. If this case was placed further from ground, the generation of downforce would be even smaller because the flow would be symmetric, and as exposed in previous sections, a symmetrical body in free stream does not generate lift. The downforce obtained is of 0.182, a rather small value considering the Formula 1 downforce requirements. As seen in Fig. 4.51 (a), two vortex generate at the rear bottom of this body. In this case both vortex are quite small, which justifies the small value of downforce obtained. The vortex are somehow constraint by the end of the body as they do not have the space to be developed. For this reason, a 25° diffuser is added to the non-diffuser Ahmed body geometry in order to observe how the presence of a diffuser improves the downforce on the body under the same conditions.

The presence of the 25° diffuser (Fig. 4.50 (b)) shows an improvement in the performance of the body when generating downforce. The downforce obtained is of 1.419, approximately 8 times more downforce than in the non-diffuser configuration. In this case, as seen in Fig. 4.51 (b), two vortex generate at the diffuser inlet with much

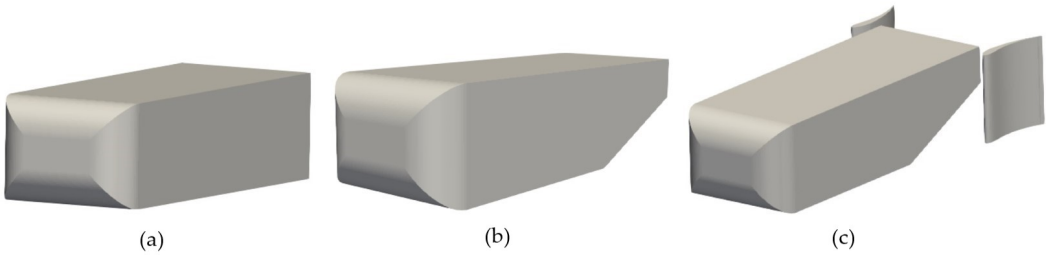

(a) (b) (c)

FIGURE 4.50: The three geometries of the Ahmed body simulated (a) 0° diffuser, (b) 25° diffuser and (c) rear airfoils 25° diffuser

	Cells	**-C_L**	C_D	ΔC_L
Non-diffuser configuration	1,108,684	0.182	0.287	-
25° diffuser configuration	1,456,999	1.419	0.558	1.237 (+680% with respect the non-diffuser configuration)
Rear airfoils configuration	1,552,709	2.14	1.08	0.721 (+51% with respect the 25° diffuser)

TABLE 4.1: Table with the results obtained for each simulation

bigger size than the ones generated on the 0° diffuser. The two symmetrical counter-rotating vortex verify the theory that stated these vortex appeared on the diffuser. Also the theory stated that the larger the size of the vortex, the larger the downforce. Thing that is clearly seen when comparing both 0° and 25° diffuser cases: the 0° diffuser cortex were small and concentrated at the bottom of the body, whereas in the 25° diffuser the vortex are much bigger in size, almost 3 times the height of the Ahmed body. As exposed in Sec. 3.7, these vortex redirect the flow upwards on the underbody and by the Newton's 3rd law, this motion upwards is the cause of the the generation of downforce acting downwards on the body. For this reason, as in this case the vortex generated are larger, their vorticity is larger, thus increasing the vertical load acting downwards on the body.

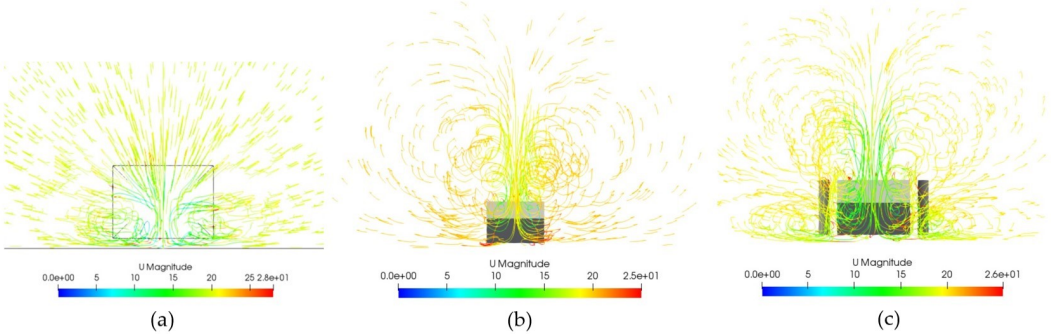

(a) (b) (c)

FIGURE 4.51: Streamlines resulted for (a) 0° diffuser, (b) 25° diffuser and (c) rear airfoils 25° diffuser

Finally, a third case proposed by Willem Toet is simulated. It consists of two airfoils added to the rear zone of the 25° diffuser Ahmed body – see Fig. 4.50 (c). The aim of simulating this case is to observe that a low pressure zone appears at the back of the body, which increases the downforce produced. From Tab. 4.1, compared to the case of the 25° diffuser configuration without airfoils, downforce has substantially

increased over 51%, as well as the drag. As in previous cases, two vortex are observed in Fig. 4.51 (c), one at each side of the diffuser. The left vortex rotates at the counterclockwise direction, while the right one rotates at the opposite direction, in the clockwise direction. Furthermore, at the bottom of the figure it seems to show another 2 vortex appear. This could be caused by the rear airfoils that guide the flow following the shape of the airfoils and make the flow on the main vortex to change its direction. The airfoils seem to help redirecting the flow more smoothly to the free stream. They also help sealing the lower pressure area at the back of the car creating a suction zone, thing that may prevent fluid loses through the sides of the car, increasing the mass flow rate entering the diffuser. From the theory, the higher the mass flow rate in the diffuser, the larger the downforce that can be produced. In conclusion, the addition of two airfoils at the back of the body signifies an improvement in the generation of downforce. Hence, adding aerodynamic elements that create a low pressure zone at the back of a car is a good technique in order to increase the downforce, for instance in Formula 1 tracks that have lots of cornering zones and need a good adhesion of the car to the ground to improve lap times. Otherwise, it must be noted that the drag coefficient is quite high, so it should be considered in order to apply this diffuser configuration, or introduce a device that reduces the drag produced.

5 Environmental impact

This projects consists of a theoretical investigation and a numerical study. As both these parts require just the use of a computer, the only environmental impact generated by this project will be power consumed. Hence, as no product is being manufactured and no experimental tests are being performed, electricity is just considered as the only factor affecting the environment. The only aspect to consider is the total hours of computer use, considering 300 W of computer power. The project time realization goal is set to 300h, thus this is the value of hours considered to have consumed electricity as an estimation of the carbon dioxide emission approximation.

Activity	**Time [h]**	**Power consumption [kWh]**	**Carbon dioxide CO_2 emission [kg]**
Computer of 300 W	300	90	38.6
TOTAL			**38.6**

TABLE 5.1: Amount of carbon dioxide CO_2 emissions

The total 300h of computer usage per the power of the computer results in 90kWh. From [5], it is approximated that the consumption of 1 kWh is equivalent to the emission of 0.429 kgs of CO_2 per kWh, thus the corresponding amount of carbon dioxide emissions are 38.61kg. This quantity may seem small but if all the people didn't worry about reducing their carbon footprint, the pollution would increase and the world's health wouldn't be better. For this reason, people should be more conscious about the climate change as it is something that affects all the inhabitants of the world, richer and poorer. Enhancing the use of renewable energies would improve the state of the planet. In Spain, as the hours of sun are predominant during all the year, the use of solar panels would be of great help.

6 Planning of the project

This project has a value of 12 ECTS, therefore, 300 hours in total. From this total hours, the tasks to be completed and the approximate hours spent on each task are presented in Table 6.1. The Gantt chart for the project is made from this table and can be found attached in Appendix **??**. The tasks A4 and D2 are represented in the Gantt chart as *Milestones*, thus representing significant events in the development of the project which highly influence the realization of the rest of the tasks. It must be highlighted that the delivery date is the **30th of June**.

Task			**Precedents**	**Hours**	
A. Project's theoretical approach	A1. Objectives and scope of the project definition		-	0.5	145
	A2. Definition of the table of contents		A1	2	
	A3. Research of information		A2	30	
	A4. Project Charter		A1, D1	2.5	
	A5. Fundamentals of aerodynamics		-	3	
	A6. Diffuser theoretical approach	A6.1. Geometry	A3	25	
		A6.2. Flow analysis	A3	37	
		A6.3. Definition of diffuser performance	A3	25	
		A6.4. Experimental research	A3	10	
		A6.5. Numerical research	A3	10	
B. CFD simulations	B1. Self-learning of Computational Fluid Dynamics (CFD)		-	65	120
	B2. Diffuser geometry determination		A6.1	5	
	B3. Boundary conditions		A6, B1	5	
	B4. Mesh determination		B2, B3	20	
	B5. CFD simulation of diffusers		B4	5	
	B6. Post-processing		B5	5	
	B7. Analysis of results		B6	15	
C. Further studies	C1. Planning of the project		A1	2.5	10.5
	C2. Budget and feasibility of the project		C1	4	
	C3. Environmental impact study		A3	4	
D. End of the project	D1. Conclusions		A, B, C	4	24.5
	D2. Final delivery of the project		D1	0.5	
	D3. Oral presentation preparation		D2	20	
TOTAL					**300**

TABLE 6.1: Table with the tasks to do and the hours spent.

The project was started following the timings exposed on the previous table and the Gantt chart. Unfortunately, all the timings couldn't be followed accurately due to external factors that affected the development of the project.

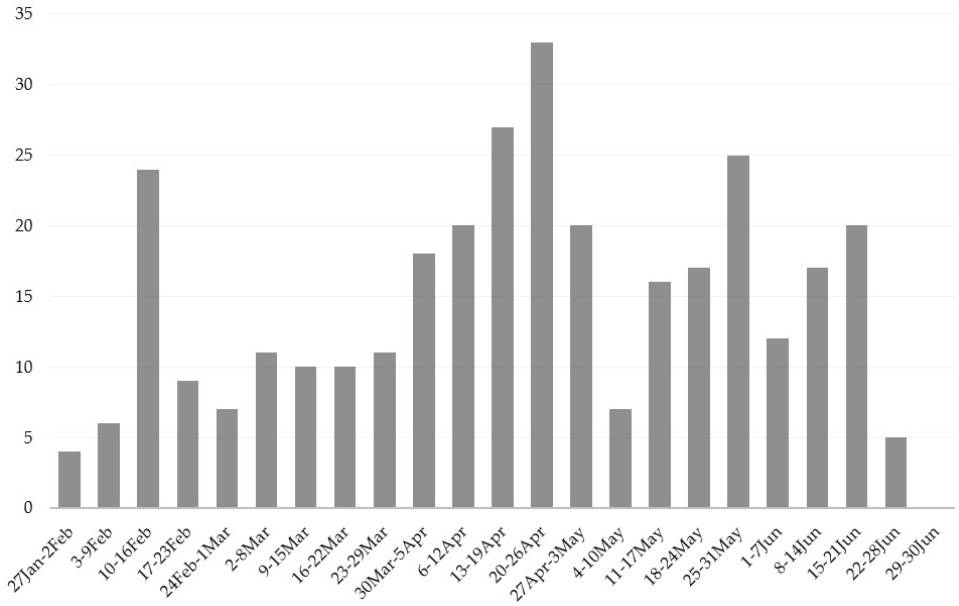

FIGURE 6.1: Hours per week spent working on the project

The hours spend per week were monitored by writing down every day the hours spent on the project each day. These hours per week are plotted in a bar chart in Fig. 6.1.

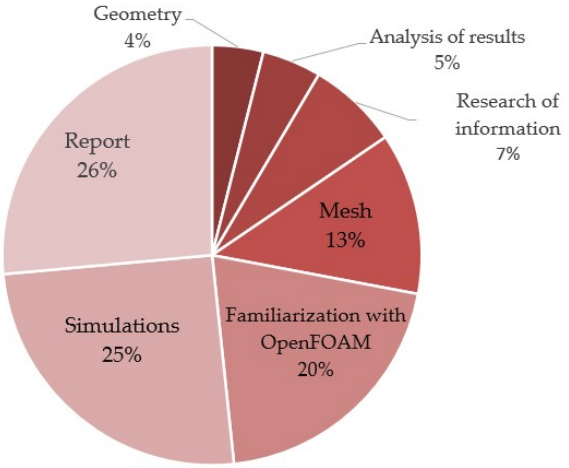

FIGURE 6.2: Percentage of the total hours spent on the main tasks done

Furthermore, the hours spent on the project exceeded the 300 hours stipulated considering the number of ECTS. The final total hours spent were of 329. From these total hours, the percentage dedicated to each task is shown in Fig. 6.2. It stands out that the most hours spent are on CFD, either on the familiarization on OpenFOAM to the realization of the simulations performed. The realization of the writing report – from the theoretical part to the CFD simulations – has the largest percentage (26%). The part of the report that took the longest to write was the theoretical part as it is one of the most important part of the project and it had to be as understandable as possible. The next task with high percentage of total hours spent is the time of simulation. The *simpleFoam* solver didn't take long to give results, but it was the transient solver *pimpleFoam* that in some simulations took over days to give the desired or stabilized results. Along with this task, the creation of the mesh also stands out as one of the most time-consuming activity –even though it has a percentage of 13%,

which may seem little. Eventually, the simulation time is the time that one has to wait to obtain results but for the mesh, the *snappyHexMeshDict* must be worked on and change the parameters until the desired mesh is obtained considering the lack of computational resources. Finally, the least time-consuming main activities were the research, reading and understanding of information, mesh creation and analysis of the results obtained.

7 Conclusions

This project has discussed how motorsport diffusers work and their importance to the performance of the car. The main objective was to understand how they flow behaves through these diffusers and how they increase the downforce acting on the vehicle. How this downforce can be increased by modifying the diffuser geometry is also studied. Furthermore, three CFD simulations are performed on three different geometries. The geometry considered is the Ahmed body, which is a usual model used to represent the flow on motorsport studies.

The flow behaviour on a motorsport diffuser may seem easy to understand, but actually it is quite hard to fully understand how it works – even senior Formula 1 aerodynamics engineers do not understand some aspects of their functioning. For this reason, in this project an extense and deep investigation about all the studies done on this aerodynamic element was done in order to understand it better and, once understood, explain the relevant aspects that govern the diffusers accurately. One important aspect of these diffusers is that their efficiency depend on the geometry parameters: **diffuser's length, slant angle and ride height**. It is concluded that diffuser's lengths near half of the whole body length show the best performance. For the slant angle, the larger the better up to a point where the flow on the diffuser's wall can detach if this angle is big enough. And regarding the ride height, as closer to the ground downforce increases. However, it occurs the same as in the slant angle: from a determined ride height very close to ground, downforce stops increasing and decreases since the flow between the body and the ground can become chocked. Furthermore, another important aspect to bear in mind is the generation of vortices at the diffuser inlet. These vortices are the most non-understood part from diffusers, even real Formula 1 aerodynimicists don't completely understand them. Two counter-rotating vortex appear at the beginning of the diffuser inlet, and depending on their size the downforce can be bigger or smaller. Usually, the bigger the vortex, the larger the downforce generated.

Once the functioning of the diffuser is studied, CFD simulations with OpenFOAM© are performed to complete the explanation. As mentioned previously, the geometry considered is the Ahmed body as it simplifies the simulation complexity. Three cases at a ride height of 20 mm are studied: Ahmed body without a diffuser (slant angle of 0°), 25° diffuser and 25° diffuser with the addition of two rear airfoils, one at each side of the diffuser. The three simulations performed show reasonable results. From least to most downforce generated, the non-diffuser Ahmed body results in the least downforce generation configuration compared to the 2 other cases, followed by the 25° and finally the large downforce produced is by adding the rear airfoils to the 25° diffuser configuration. It must be highlighted that with the increase of lift coefficient, the drag increases consequently. The case of the non-diffuser Ahmed body shows the least downforce generation ($C_L = -0.18$), as theory predicted. For the 25° diffuser configuration, the downforce increases substantially with respect the non-diffuser configuration up to obatining lift coefficient of approximately -1.42,

8 times more than the 0° diffuser. Last but not least, the simulation of the case of the 25° diffuser Ahmed body with the addition of two rear airfoils was proposed by former Formula 1 aerodynamics engineer Willem Toet to create a suction zone at the back of the Ahmed body with the aim of increasing the downforce. Effectively, the downforce obtained for this last case was significantly larger to the second case with just the 25° diffuser. The lift coefficient resulted in -2.14, 51% more downforce with the addition of the airfoils. The region of low pressure at the back of the body could be clearly observed, thing that enables a smoother transition of the flow leaving the diffuser.

In conclusion, the main objectives of the project are achieved, as described below.

- **Acknowledge in detail the use and importance of diffusers in Formula 1 cars.** Now the functioning and importance of diffusers are more clear, knowing all the aspects that govern these aerodynamic elements and how the geometry must be varied in order to improve the performance.
- **Learn to use CFD thoroughly.** Even though CFD is rather difficult to learn in such short time, it has been acknowledge its basics and how it works. Nevertheless, in just 4 months it has been learned how to introduce the right boundary conditions along with the required parameters for the simulation considering the turbulence model used. A better understanding of turbulence model and the corresponding equations is known. The simulations conditions are also learned to be applied. Furthermore, a post-process stage is done using the software tools available.
- **Explain clearly the obtained results so that a Formula 1 fan who is not an aerodynamics expert can understand the concepts explained.** The functioning of the diffuser is explained with clear explanations and figures that ease the understanding of these devices. Regarding the CFD simulations, it may appear hard to understand to a non-expert profile. However, they are analyzed and discussed as accurate as possible.
- **Work in the study and analysis of fluid simulations involving real engineering problems.** Three different geometries are simulated and a comparison between the results obtained is done. One aspect to highlight about the CFD simulations is that the process of meshing the geometry was underestimated. This process seems easy, but in complex geometries it gets more complicated with a time consumption on the mesh creation was larger than expected.
- **Determine feasibility of the engineering project to be carried out.** A budget is done obtaining a total cost of 6787€ applying a price per hour of 15€. An environmental impact study of the project is done resulting in 38.6 kg of CO_2 emissions due to the use of electric energy of the computer.
- **Study the socio-economics aspects in fluid dynamics applications solved by numerical simulation and fields of interest.** CFD simulations are not only used to improve the downforce acting on a car, but it is also used to improve fuel consumption, lubrication of pieces of the engine, etc. For this reason, numerical simulations are interesting to apply in different fields of study, not only on vehicles, so as to optimize resources.

Regarding the planning of the project, there were some complications due to external factors that affected the realization of the project. Nevertheless, this complications were overcome and the project was finished successfully.

Bibliography

[1] Mohd Radzi Abu Mansor and Zambri Harun. "F1 in SCHOOLS Competition to Promote STEM: Aerodynamic Investigation of Miniature F1 in SCHOOLS Car". In: *Proceedings - 2017 7th World Engineering Education Forum, WEEF 2017- In Conjunction with: 7th Regional Conference on Engineering Education and Research in Higher Education 2017, RCEE and RHEd 2017, 1st International STEAM Education Conference, STEAMEC 201* (2018), pp. 708–712. DOI: 10.1109/WEEF.2017.8467172.

[2] S. R. Ahmed, G. Ramm, and G. Faltin. "Some salient features of the time-averaged ground vehicle wake". In: *SAE Technical Papers*. SAE International, 1984. DOI: 10.4271/840300.

[3] Gautham Barathwaj. *What is the effect of adverse pressure gradient on boundary layer separation?* 2018. URL: https://www.quora.com/What-is-the-effect-of-adverse-pressure-gradient-on-boundary-layer-separation (visited on 05/03/2020).

[4] *Boundary Layer*. URL: https://www.nuclear-power.net/nuclear-engineering/fluid-dynamics/boundary-layer/ (visited on 05/03/2020).

[5] Carbonfund.org. *Carbon and Usage Calculation Methods*. 2018. URL: https://carbonfund.org/calculation-methods/ (visited on 06/10/2020).

[6] CFD-Wiki. *Turbulence intensity – {CFD-Wiki}, the free {CFD} reference*. 2013. URL: http://www.cfd-online.com/Wiki/Turbulence{_}intensity (visited on 04/26/2020).

[7] Kevin R. Cooper, J. Syms, and G. Sovran. "Selecting automotive diffusers to maximise underbody downforce". In: *SAE Technical Papers* (2000). ISSN: 26883627. DOI: 10.4271/2000-01-0354.

[8] Kevin R. Cooper et al. "The aerodynamic performance of automotive underbody diffusers". In: *SAE Technical Papers* 107 (1998), p. 150. ISSN: 26883627. DOI: 10.4271/980030.

[9] *Diffusers - an overview*. URL: https://www.sciencedirect.com/topics/engineering/diffusers (visited on 02/14/2020).

[10] *Downforce vs. drag*. URL: http://www.formula1-dictionary.net/Big/downforce{_}vs{_}drag{_}big.png (visited on 05/03/2020).

[11] O. H. Ehirim, K. Knowles, and A. J. Saddington. "A review of ground-effect diffuser aerodynamics". In: *Journal of Fluids Engineering, Transactions of the ASME* 141.2 (2018). ISSN: 1528901X. DOI: 10.1115/1.4040501.

[12] Jousef Murad. *Defining Turbulent Boundary Conditions*. URL: https://www.simscale.com/forum/t/defining-turbulent-boundary-conditions/80895 (visited on 03/14/2020).

[13] Ali Asgar S. Khokhar and Suhas S. Shirolkar. "Design and Analysis of Undertray Diffuser for a Formula Style Racecar". In: *International Journal of Research in Engineering and Technology* 04.11 (2015), pp. 202–210. ISSN: 23217308. DOI: 10.15623/ijret.2015.0411035.

[14] Jason Knight et al. "Investigation of vehicle ride height and diffuser ramp angle on downforce and efficiency". In: *Proceedings of the Institution of Mechanical Engineers, Part D: Journal of Automobile Engineering* 233.8 (2019), pp. 2139–2145. ISSN: 09544070. DOI: 10.1177/0954407018776767.

[15] Amrit Kumar. *Types of Fluid Flow*. URL: https://learnmechanical.com/types-of-fluid-flow/ (visited on 05/03/2020).

[16] Salvador Mayoral, Hope Weiss, and Ramitha Edirisinghe. "On the relationship between the vortices from an underbody diffuser in ground-effect and the resulting downforce". In: *SAE Technical Papers*. Vol. 2019-April. April. SAE International, 2019. DOI: 10.4271/2019-01-0650.

[17] Jousef Murad. *Ahmed Body*. URL: https://www.simscale.com/forum/t/ahmed-body/64235 (visited on 04/15/2020).

[18] OpenCFD. *k-Omega Shear Stress Transport (SST)*. 2017. URL: https://www.openfoam.com/documentation/guides/latest/doc/guide-turbulence-ras-k-omega-sst.html (visited on 05/10/2020).

[19] Oriol. *Partes y características de un fondo plano de un Formula 1*. 2018. URL: https://www.formula1atmosphere.com/wp-content/uploads/2018/08/undertray{_}underbody.png (visited on 02/11/2020).

[20] Kevin M Peddie and Luis F Gonzalez. *CFD Study on the Diffuser of a Formula 3 Racecar*. Tech. rep. 1. Sydney: University of Sydney, 2004, pp. 18–35.

[21] Andrea E. Senior and Xin Zhang. "The force and pressure of a diffuser-equipped bluff body in ground effect". In: *Journal of Fluids Engineering, Transactions of the ASME* 123.1 (2001), pp. 105–111. ISSN: 1528901X. DOI: 10.1115/1.1340637.

[22] *Separation of Flow*. 2005. URL: http://www-mdp.eng.cam.ac.uk/web/library/enginfo/aerothermal{_}dvd{_}only/aero/fprops/introvisc/node9.html (visited on 05/03/2020).

[23] John Southard. *Boundary Layers*. 2019. URL: https://geo.libretexts.org/Bookshelves/Sedimentology/Book{\%}3A{_}Introduction{_}to{_}Fluid{_}Motions{_}and{_}Sediment{_}Transport{_}(Southard)/03{\%}3A{_}Flow{_}Past{_}a{_}Sphere{_}II{_}-{_}Stokes'{_}Law{\%}2C{_}The{_}Bernoulli{_}Equation{\%}2C{_}Turbulence{\%}2C{_}Boundary{_}Layers{\%}2C{_}Flow{_}Separation/3.06{\%}3A{_}Bo (visited on 05/03/2020).

[24] Eric Tingwall. *The Physics of Diffusers: How to Make a Car Really Suck*. 2013. URL: https://www.caranddriver.com/features/a15112568/the-physics-of-diffusers-how-to-make-a-car-really-suck-feature/ (visited on 02/06/2020).

[25] *Undertray or Underbody*. 2017. URL: http://www.formula1-dictionary.net/undertray.html (visited on 02/18/2020).

[26] *Vortex*. URL: http://www.formula1-dictionary.net/vortex.html (visited on 05/04/2020).

[27] Willem Toet. *How do motorsport diffusers work?* 2015. URL: https://www.linkedin.com/pulse/how-do-motorsport-ground-effect-diffusers-work-willem-toet (visited on 02/14/2020).

[28] X. Zhang, A. Senior, and A. Ruhrmann. "Vortices behind a bluff body with an upswept aft section in ground effect". In: *International Journal of Heat and Fluid Flow* 25.1 (2004), pp. 1–9. ISSN: 0142727X. DOI: 10.1016/j.ijheatfluidflow.2003.11.002.